MIT Libraries | DSpace@MIT

MIT Open Access Articles

A MULTIWAVELENGTH STUDY OF THE HIGH SURFACE BRIGHTNESS HOT SPOT IN PKS 1421–490

Massachusetts Institute of Technology

A MULTIWAVELENGTH STUDY OF THE HIGH SURFACE BRIGHTNESS HOT SPOT IN PKS 1421−490

L. E. H. Godfrey[1,2], G. V. Bicknell[1], J. E. J. Lovell[2,3,4], D. L. Jauncey[2], J. Gelbord[5], D. A. Schwartz[6], H. L. Marshall[7],
M. Birkinshaw[6,8], M. Georganopoulos[9,10], D. W. Murphy[11], E. S. Perlman[9], and D. M. Worrall[6,8]
[1] Research School of Astronomy and Astrophysics, Australian National University, Cotter Road, Weston, ACT, 2611, Australia; lgodfrey@mso.anu.edu.au
[2] Australia Telescope National Facility, CSIRO, P.O. Box 76, Epping, NSW, 2121, Australia
[3] CSIRO, Industrial Physics, PO Box 218 Lindfield NSW 2070, Australia
[4] School of Mathematics and Physics, University of Tasmania, Tas 7001, Australia
[5] Department of Physics, Durham University, South Road, Durham, DH1 3LE, UK
[6] Harvard-Smithsonian Center for Astrophysics, 60 Garden Street, Cambridge, MA 02138, USA
[7] Kavli Institute for Astrophysics and Space Research, Massachusetts Institute of Technology, USA
[8] Department of Physics, University of Bristol, Tyndall Avenue, Bristol BS8 1TL, UK
[9] Department of Physics, Joint Center for Astrophysics, University of Maryland-Baltimore County, 1000 Hilltop Circle, Baltimore, MD 21250, USA
[10] NASA Goddard Space Flight Center, Mail Code 660, Greenbelt, MD 20771, USA
[11] Jet Propulsion Laboratory, 4800 Oak Grove Drive, Pasadena, CA 91109, USA

ABSTRACT

Long Baseline Array imaging of the $z = 0.663$ broadline radio galaxy PKS 1421−490 reveals a 400 pc diameter high surface brightness hot spot at a projected distance of ∼40 kpc from the active galactic nucleus. The isotropic X-ray luminosity of the hot spot, $L_{2-10\,keV} = 3 \times 10^{44}$ ergs s^{-1}, is comparable to the isotropic X-ray luminosity of the entire X-ray jet of PKS 0637−752, and the peak radio surface brightness is hundreds of times greater than that of the brightest hot spot in Cygnus A. We model the radio to X-ray spectral energy distribution using a one-zone synchrotron self-Compton model with a near equipartition magnetic field strength of 3 mG. There is a strong brightness asymmetry between the approaching and receding hotspots and the hot spot spectrum remains flat ($\alpha \approx 0.5$) well beyond the predicted cooling break for a 3 mG magnetic field, indicating that the hotspot emission may be Doppler beamed. A high plasma velocity beyond the terminal jet shock could be the result of a dynamically important magnetic field in the jet. There is a change in the slope of the hotspot radio spectrum at GHz frequencies, which we model by incorporating a cutoff in the electron energy distribution at $\gamma_{min} \approx 650$, with higher values implied if the hotspot emission is Doppler beamed. We show that a sharp decrease in the electron number density below a Lorentz factor of 650 would arise from the dissipation of bulk kinetic energy in an electron/proton jet with a Lorentz factor $\Gamma_{jet} \gtrsim 5$.

Key words: galaxies: active – galaxies: jets – quasars: individual (PKS 1421−490)

1. INTRODUCTION

PKS 1421−490 was first reported as a bright, flat spectrum radio source by Ekers (1969). Subsequent Very Long Baseline Interferometry (VLBI) revealed 10 mas scale structure within the brightest component of this source (Preston et al. 1989). Studies at the Australia Telescope Compact Array (ATCA) later revealed significant radio emission on arcsecond scales extending southwest from the brightest component (Lovell 1997). For this reason, PKS 1421−490 was included in a *Chandra* survey of flat spectrum radio quasars with arcsecond scale radio jets (Marshall et al. 2005). Gelbord et al. (2005, from here on G05) reported on recent X-ray (*Chandra*), optical (Magellan), and radio (ATCA) imaging of this source. We refer the reader to that paper for the details of these observations and images.

Figure 1 illustrates the arcsecond scale radio structure of PKS 1421−490; it is annotated to show the naming convention for different components in the radio image used by G05, as well as the correct interpretation of each of these components brought out in this study. G05 obtained an optical spectrum of region B, and suggested it was not associated with an active galactic nucleus (AGN) in view of the apparent lack of spectral lines (due to a poor signal-to-noise ratio in that spectrum). Region A was known to contain bright VLBI scale radio structure (Preston et al. 1989) and had a flat radio spectrum ($\alpha < 0.5$). Consequently region A was thought to be an AGN, while region B was (erroneously) interpreted by G05 as a jet knot. In this paper, we show that in fact region B is the AGN (see Section 3), and that region A contains a high surface brightness hot spot. The main focus of this paper is the interpretation and modeling of the exceptional hot spot in region A which has until now been interpreted as an AGN.

One of the major results of this paper relates to an observed low-frequency flattening in the hotspot radio spectrum at GHz frequencies, which indicates that the underlying electron energy distribution flattens toward lower energies. The low-energy electron distribution is not only important for calculating parameters such as the number density and energy density, it also provides important constraints on the particle acceleration mechanism. In turn, this will help us to address more fundamental issues such as jet composition and speed. We now present a brief overview of the literature relating to the low-energy electron distribution in jets and hotspots.

In a small number of objects, flattening of the hotspot radio spectra toward lower frequencies has been observed. In most cases, synchrotron self-absorption and free–free absorption can be ruled out, and the observed flattening is interpreted in terms of a turnover in the electron energy distribution (Leahy et al. 1989; Carilli et al. 1988, 1991; Lazio et al. 2006). When modeling hotspot spectra, the turnover in the electron energy distribution is usually approximated by setting the electron number density equal to zero below a cutoff Lorentz factor γ_{min}. In each case where flattening of the hotspot radio spectrum has been directly observed, estimates of γ_{min} are of the order of several hundred:
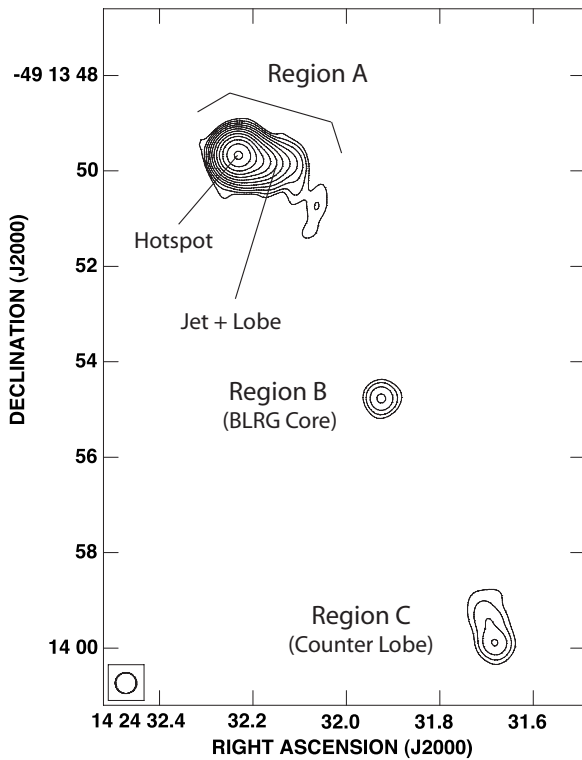
Figure 1. ATCA 20.2 GHz image of PKS 1421−490 with source components labeled. This image was first presented in G05. To avoid confusion, the naming convention used by G05 is also included. Contour levels: 1.5 mJy beam^{-1} × (1, 2, 4, 8, 16, 32, 64, 128, 256, 512, 1024). Peak surface brightness: 2.11 Jy beam^{-1}. Beam FWHM: 0.54 × 0.36 arcsec. The scale of the image is 7.0 kpc arcsecond^{-1}.

Cygnus A, $\gamma_{min} \sim 300$–400 (Carilli et al. 1991; Lazio et al. 2006; Hardcastle 2001); 3C295, $\gamma_{min} \sim 800$ (Harris et al. 2000; Hardcastle 2001); 3C123, $\gamma_{min} \sim 1000$ (Hardcastle et al. 2001; Hardcastle 2001); PKS 1421−490, $\gamma_{min} \sim 650$ (this work).

Leahy et al. (1989) presented evidence for a low-energy cutoff in two other hot spots: 3C268.1 and 3C68.1. In both these objects, the hotspot radio spectra are significantly flatter between 150 MHz and 1.5 GHz than they are above 1.5 GHz, which suggests a similar value of γ_{min} to those listed above, provided the hotspot magnetic field strengths are similar. More recently, Hardcastle (2001) reported on a possible detection of an optical inverse Compton hot spot in the quasar 3C196. By modeling the synchrotron self-Compton (SSC) emission and assuming a magnetic field strength close to the equipartition value, they inferred a cutoff Lorentz factor $\gamma_{min} \sim 500$. All of the above listed, γ_{min} estimates appear to be distributed around a value of $\gamma_{min} \sim 600$. However, Blundell et al. (2006) and Erlund et al. (2008) have inferred the existence of a low-energy cutoff at $\gamma_{min} \gtrsim 10^4$ in the hotspots of the giant radio galaxy 6C 0905−3955. Their method of detecting the low-energy cutoff is quite different to those described above, and is based on the interpretation of the absence of X-ray emission from the eastern hot spot and radio lobe in that source.

In Section 8, we show that a turnover in the electron energy distribution at $\gamma_{min} \sim 100$–1000 can arise naturally from dissipation of jet energy if the jet has a high proton fraction and a bulk Lorentz factor $\Gamma_{jet} \gtrsim 5$. However, Stawarz et al. (2007) have suggested that the low-frequency flattening in the radio spectrum of a Cygnus A hot spot is not related to the turnover

in electron energy distribution. Rather, they argue, it indicates a transition between two different acceleration mechanisms.

Electron energy distributions with a low-energy cutoff have also been discussed in relation to pc-scale jets. The absence of significant Faraday depolarization in compact sources suggests that the number density of electrons with Lorentz factor $\gamma \gtrsim 100$ greatly exceeds that of lower energy particles (Wardle 1977; Jones & Odell 1977). Gopal-Krishna et al. (2004) have argued that some statistical trends in superluminal pc-scale jets may be understood in terms of effects arising from a low-energy cutoff in the electron energy distribution. Tsang & Kirk (2007) have suggested that a low-energy cutoff in the electron spectrum can alleviate several theoretical difficulties associated with the inverse Compton catastrophe in compact radio sources, including anomalously high brightness temperatures and the apparent lack of clustering of powerful sources at 10^{12} K. However, circular polarization in the pc-scale jet of 3C279 requires a minimum Lorentz factor $\gamma_{min} < 20$ (Wardle et al. 1998).

Observational constraints on the low-energy electron distribution in extragalactic jets on kpc-scales are rare. A low-energy cutoff in the electron energy distribution at $\gamma_{min} \sim 20$ has been estimated for the jet of PKS 0637−752 (500 kpc from the nucleus) through modeling of the radio to X-ray spectral energy distribution in terms of inverse Compton scattering of the cosmic microwave background (CMB; Tavecchio et al. 2000; Uchiyama et al. 2005).

This paper is structured as follows. In Section 2, we discuss our observations and data reduction. In Section 3, we discuss the AGN—in particular the optical spectrum and broadband spectral energy distribution. In Section 4, we present the VLBI image of the northern hot spot and derive plasma parameters by modeling the broadband spectral energy distribution. In Section 5, we independently estimate the hotspot plasma parameters by modeling the radio spectrum of the entire radio galaxy. In Section 6, we discuss the incompatibility of the observed spectrum with the standard continuous injection plus synchrotron-cooling model for hotspots. In Section 7, we consider Doppler beaming as a possible cause of the high radio surface brightness and various other properties of the hot spot. In Section 8, we consider the dissipation of energy associated with a cold proton/electron jet and present an expression that relates the energy of the peak in the electron energy distribution to the jet bulk Lorentz factor. We then consider the implications of this expression in the case of the northern hot spot of PKS 1421−490 and other objects. In Section 9, we summarize our findings.

Throughout this paper, we assume cosmology $\Omega_\Lambda = 0.73$, $\Omega_M = 0.27$, $H_0 = 71$ km s^{-1} Mpc^{-1}, and we define the spectral index as $\alpha = -\frac{\log(F_1/F_2)}{\log(\nu_1/\nu_2)}$ so that the flux density $F_\nu \propto \nu^{-\alpha}$.

2. OBSERVATIONS AND DATA REDUCTION

2.1. Summary

We observed PKS1421−490 with the Long Baseline Array (LBA) at 2.3 and 8.4 GHz and with the ATCA at 2.3, 4.8, 8.4, and 93.5 GHz. We have also made use of ATCA radio data (4.8, 8.6, 17.7, and 20.2 GHz) previously published in Gelbord et al. (2005) as well as archival 1.4 GHz ATCA data. We combined these data with previously published infrared, optical and X-ray flux densities to construct radio to X-ray spectra for the northern hot spot and the core as well as an accurate radio spectrum of the entire radio galaxy. Table 1 lists the observation information

Table 1
Observation Information and Flux Densities

Flux Density of...	Instrument	Frequency	Date Observed	Configuration	Resolution[a]	Flux Density (Jy)	Reference
Entire Source	MOST	408 MHz	1968–1978	· · ·	2′.8	13.1 ± 0.7	1
Entire Source	Parkes	468 MHz	1965–1969	· · ·	54′	11.9 ± 0.1	2
Entire Source	Parkes	635 MHz	1965–1969	· · ·	30′.5	10.9 ± 0.5	2
Entire Source	MOST	843 MHz	1990–1993	· · ·	1′.1	9.9 ± 0.5	3
Entire Source	ATCA	1.38 GHz	2000 Feb 24	6A[b]	2″.2 [c]	8.5 ±0.2	4
Entire Source	ATCA	2.28 GHz	2006 Mar 23	6C[b]	3′[c]	7.15 ± 0.15	4
Entire Source	ATCA	4.80 GHz	2005 May 19	H168	3′.5 [c]	5.5 ± 0.1	4
Entire Source	ATCA	8.425 GHz	2005 May 19	H168	2′[c]	4.25 ± 0.1	4
Entire Source	ATCA	8.64 GHz	2002 Feb 4	6C[b]	47″[c]	4.1 ± 0.1	4
Entire Source	ATCA	17.73 GHz	2004 May 9	6C[b]	30″[c]	2.74 ± 0.06	4
Entire Source	ATCA	20.16 GHz	2004 May 9	6C[b]	26″[c]	2.54 ± 0.05	4
Entire Source	ATCA	93.5 GHz	2005 Aug 21	H214[b]	10″[c]	1.0 ± 0.1	4
Northern Hotspot	LBA	2.28 GHz	2006 Mar 23	Tidbinbilla, ATCA Mopra, Parkes Hobart, Ceduna	13.5×11.6 mas	4.25 ± 0.2	4
Northern Hotspot	LBA	8.425 GHz	2005 May 19	Parkes, Mopra, ATCA	33×13 mas	$3.2\,^{+0.2}_{-0.3}$	4
Northern Hotspot	ATCA	17.73 GHz	2004 May 9	6C	$0''.58 \times 0''.43$	< 2.3	4
Northern Hotspot	ATCA	20.16 GHz	2004 May 9	6C	$0''.51 \times 0''.37$	< 2.1	4
Northern Hotspot	ATCA	93.5 GHz	2005 Aug 21	H214	10″[c]	$0.8 < F_{93.5\,\mathrm{GHz}} < 1.1$[d]	4
Northern Hotspot	2MASS	1.38×10^{14} Hz	1998–2001	· · ·	~4″	$< 3.7 \times 10^{-4}$	5
Northern Hotspot	2MASS	1.82×10^{14} Hz	1998–2001	· · ·	~4″	$< 2.7 \times 10^{-4}$	5
Northern Hotspot	2MASS	2.4×10^{14} Hz	1998–2001	· · ·	~4″	$< 2.1 \times 10^{-4}$	5
Northern Hotspot	Magellan	3.93×10^{14} Hz	2003 Apr 26	MagIC	~0″.6	$(3.9 \pm 0.8) \times 10^{-6}$	5
Northern Hotspot	Magellan	4.82×10^{14} Hz	2003 Apr 26	MagIC	~0″.6	$(3.0 \pm 0.9) \times 10^{-6}$	5
Northern Hotspot	Magellan	6.29×10^{14} Hz	2003 Apr 26	MagIC	~0″.6	$(1.9 \pm 0.8) \times 10^{-6}$	5
Northern Hotspot	Chandra	2.41×10^{17} Hz	2004 Jan 16	ACIS-S	0″.5	$(1.3 \pm 0.16) \times 10^{-8}$	5
Core	ATCA	4.8 GHz	2002 Feb 4	6C		$< 7 \times 10^{-3}$	5
Core	ATCA	8.64 GHz	2002 Feb 4	6C		$(9.6 \pm 0.6) \times 10^{-3}$	5
Core	ATCA	17.73 GHz	2004 May 9	6C		$(9.8 \pm 0.3) \times 10^{-3}$	5
Core	ATCA	20.16 GHz	2004 May 9	6C		$(9.2 \pm 0.2) \times 10^{-3}$	5
Core	2MASS	1.38×10^{14} Hz	1998–2001	· · ·	~4″	$(1.00 \pm 0.07) \times 10^{-3}$	5
Core	2MASS	1.82×10^{14} Hz	1998–2001	· · ·	~4″	$(8.8 \pm 0.6) \times 10^{-4}$	5
Core	2MASS	2.4×10^{14} Hz	1998–2001	· · ·	~4″	$(9.1 \pm 0.7) \times 10^{-4}$	5
Core	Magellan	3.93×10^{14} Hz	2003 Apr 26	MagIC	~0″.6	$(8 \pm 1) \times 10^{-4}$	5
Core	Magellan	4.82×10^{14} Hz	2003 Apr 26	MagIC	~0″.6	$(8 \pm 1.5) \times 10^{-4}$	5
Core	Magellan	6.29×10^{14} Hz	2003 Apr 26	MagIC	~0″.6	$(7 \pm 2) \times 10^{-4}$	5
Core	Chandra	2.41×10^{17} Hz	2004 Jan 16	ACIS-S	0″.5	$(4.9 \pm 0.3) \times 10^{-8}$	5

Notes. Uncertainties in ATCA flux density are dominated by the uncertainty in the absolute flux calibration, which is estimated to be 2%, except for 93.5 GHz, where the uncertainty is estimated to be 10%. The lower limit on the hotspot flux at 93.5 GHz comes from making an assumption about the nonhotspot spectrum extrapolated to higher frequencies from 8.4 GHz. See Section 2.4 for details.
References. (1) Large et al. (1981); (2) Wills (1975); (3) Campbell-Wilson & Hunstead (1994); (4) This work; (5) Gelbord et al. (2005).
[a] Convert to linear resolution using 7.0 kpc arcsec^{-1}.
[b] Only short baselines on which the radio galaxy is unresolved were used to measure the flux density.
[c] Resolution of shortest baseline.
[d] See Section 2.4.

and references for all data used in this study. Figure 2 presents the spectra and indicates the source of each data point.

In addition to these data, we obtained an optical spectrum of region B in order to confirm the classification of that region as an AGN. The spectroscopic observations are described in Section 2.5.

As well as describing the observations and data reduction steps, this section includes a description of some nonstandard procedures that were required to construct the hotspot radio spectrum. Specifically, nonstandard procedures were required to determine the hotspot flux density from the 8.4 GHz LBA data set due to limited (u, v) coverage. These nonstandard procedures are described in Section 2.2.3. Nonstandard procedures were also used to obtain a lower limit to the hotspot flux density at 93.5 GHz. This procedure is described in Section 2.4.

2.2. VLBI

2.2.1. LBA Observations at 2.3 GHz

PKS 1421−490 was observed with six elements (ATCA, Mopra, Parkes, Tidbinbilla 70m, Hobart, and Ceduna) of the Long Baseline Array (LBA) on 2006 March 23. A full 12 hr synthesis was obtained, recording a single 16 MHz bandwidth with both left- and right-hand circular polarizations. Regular scans on a nearby phase calibrator, PKS 1424−418, were scheduled throughout the observation, as well as scans on a point-like source, PKS 1519−273 (Linfield et al. 1989), used for gain calibration. Unfortunately, due to hardware issues, we were only able to process right-hand circular polarization. However, this will not affect our results as we do not expect the hotspot emission to be significantly circularly polarized.
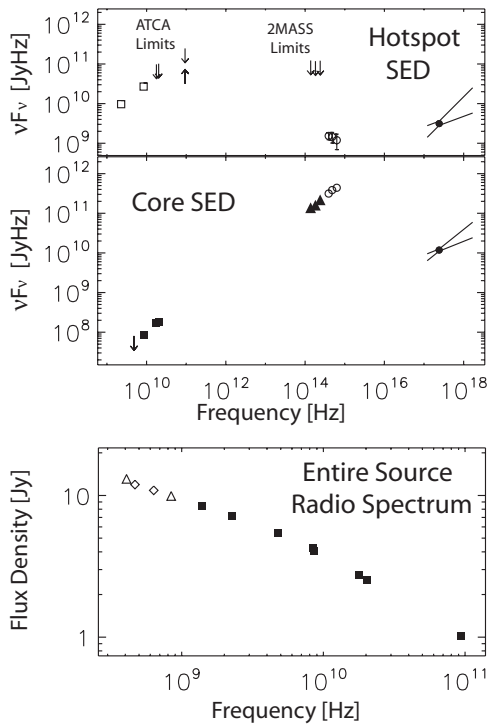
Figure 2. SED of the core and northern hot spot of PKS 1421−490, as well as the radio spectrum of the entire radio galaxy. Symbols indicate the source of the data as follows. Filled squares, ATCA; open squares, LBA; open circles, Magellan (taken from G05); filled triangles, 2MASS (taken from G05); open triangles, MOST (taken from Large et al. 1981 and Campbell-Wilson & Hunstead 1994), open diamonds, Parkes (taken from Wills 1975); filled circles, Chandra (taken from G05). The solid lines through the filled circles indicate the 1σ range of X-ray spectral index permitted by the Chandra data. Tips of arrows mark upper and lower limits (see Section 2.4 for discussion of methods used to obtain ATCA limits). Symbol sizes are greater than or approximately equal to error bars except for those points where error bars have been plotted.

Circular polarization in AGN seldom exceeds a few tenths of 1% (Rayner et al. 2000). Data were recorded to VHS tapes using the S2 system and correlated using the LBA hardware correlator with 32 channels and 2 s integration time. The data were correlated twice: once with the phase-tracking center located at the position of the radio peak in region A, and once with the phase-tracking center located ∼5 arcsec away, at the position of the core (region B).

The initial calibration of the visibility amplitudes was performed in AIPS, using the measured system temperatures and antenna gains. We obtained simultaneous ATCA data during our observation, and this allowed us to bootstrap the LBA flux scale to the ATCA flux scale by comparing simultaneous measurements of the point-like source PKS 1519−273. After scaling the gains using this bootstrapping method and correcting the residual delays and rates via fringe fitting, the data set from the phase reference source was exported to DIFMAP (Shepherd 1997) where it was edited and imaged. Amplitude and phase self-calibration corrections obtained from imaging the phase reference source were imported into AIPS using the *cordump*[12] patch kindly supplied to us by Emil Lenc. These phase and amplitude corrections were then applied to PKS 1421−490, and the data exported to DIFMAP for deconvolution and self-calibration. The resulting image is shown in Figure 3. We mea-

sure a hotspot flux density of 4.25 ± 0.2 Jy at 2.3 GHz. Preston et al. (1989) obtained a flux density of 4.1 Jy at 2.3 GHz for the northern hot spot by model fitting Southern Hemisphere VLBI Experiment (SHEVE) data with the simplest model consistent with the data (two circular Gaussians).

We attempted to detect a compact structure within region B (the core) using the data set that had been correlated with the phase center at that position. The time-averaging- and bandwidth-smeared emission from region A in this data set was first cleaned to remove the side lobes, but we were unable to detect any emission from the location of the core to a limit of ∼8 mJy (5σ). The upper limit to the flux density of region B at 4.8 GHz is 7 mJy (Gelbord et al. 2005)

2.2.2. LBA Observations at 8.4 GHz

PKS 1421−490 was observed with five elements of the LBA (ATCA, Mopra, Parkes, Hobart, and Ceduna) in 2005 May at 8.4 GHz. A full 12 hr synthesis was obtained, recording a single 16 MHz bandwidth with both the left- and right-hand circular polarizations. At this frequency, the northern hot spot of PKS 1421−490 is completely resolved on all but the shortest three baselines (baselines between Parkes, the ATCA, and Mopra). We fringe fitted our target source data using a point source model in AIPS, before performing model-fitting and phase self-calibration iterations in DIFMAP.

2.2.3. Determination of Hotspot Flux Density from the 8.4 GHz LBA Data Set

Due to the small number of baselines, we use model-fitting in the (u, v) plane rather than CLEAN deconvolution to measure the hotspot flux density at 8.4 GHz. Model-fitting involves specifying a starting model in the image plane, consisting of a number of elliptical Gaussian components, each with a particular flux density, position, size, and position angle, then allowing the model-fitting algorithm to locate a chi-squared minimum by fitting the Fourier transform of the model to the (u, v) data.

Care is necessary when comparing the LBA flux density measurements at the two different frequencies, due to the limited (u, v) coverage. At 2.3 GHz, the data cover (u, v) spacings between 0.5 and 13 Mλ, while at 8.4 GHz the data cover (u, v) spacings between 2 and 9 Mλ. Therefore, provided the source structure can be described by a simple model consisting of a set of Gaussian components, the comparison of model flux densities will be valid.

In order to determine the range of allowable flux densities in the 8.4 GHz data set, we specified a wide range of different models consisting of three, four or five elliptical Gaussian components, broadly consistent with the 2.3 GHz image, then let the model-fitting algorithm adjust the model to fit the 8.4 GHz data. While it is not possible to precisely constrain the flux density of the hot spot with only three baselines, we found that the total flux density of all acceptable models (using between three and five elliptical Gaussian components and a wide range of initial model parameters) was never less than 2.9 Jy, and the flux density of the best-fitting model was 3.2 Jy. The 8.6 GHz ATCA image contains an unresolved source of 3.3 Jy at the position of the hot spot, and this provides an upper limit to the hotspot flux density at 8.6 GHz. We therefore adopt a hotspot flux density at 8.4 GHz of $F_{8.4\,\mathrm{GHz}} = 3.2^{+0.2}_{-0.3}$ Jy.

---

[12] The *cordump* patch is available for DIFMAP at http://astronomy.swin.edu.au/∼elenc/DifmapPatches/

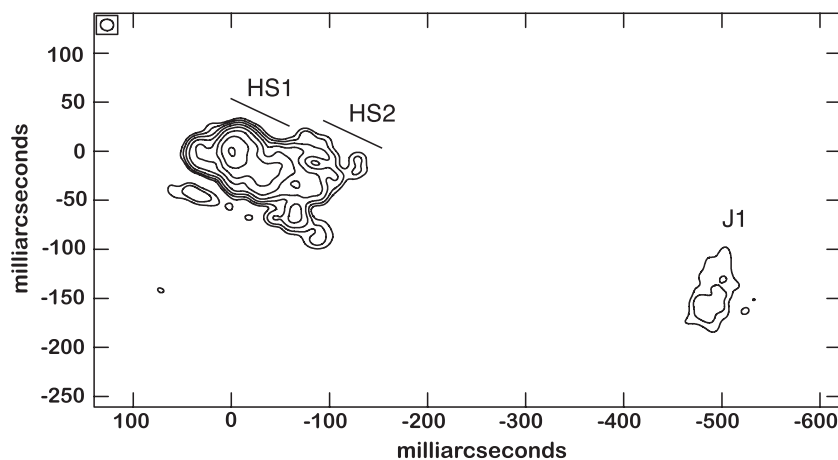**Figure 3.** VLBI image of the northern hot spot of PKS 1421−490 at 2.3 GHz. Contour levels: 3.5 mJy beam^{-1} × (1, 2, 4, 8, 16, 32, 64, 128). Peak surface brightness: 0.47 Jy beam^{-1}. Beam FWHM: 13.5 mas × 11.6 mas. The scale of this image is 7.0 pc mas^{-1}.

2.3. ATCA Observations

ATCA observations of PKS 1421−490 were made simultaneously during our LBA observations. We recorded a single 64 MHz bandwidth at 8.4 GHz and 128 MHz bandwidth at 4.8 GHz during our first LBA observation in 2005. A single 128 MHz bandwidth at 2.3 GHz was recorded during our second LBA observation in 2006. For each of these observations, the ATCA was in a compact configuration, so we could not image the source in detail, but we were able to obtain accurate total source flux density measurements (see Table 1). Total source flux density measurements were also obtained at 1.4 GHz using archival ATCA data. Standard calibration and imaging procedures were used with the MIRIAD processing software.

In 2005 August, we obtained a full 12 hr synthesis with the new 3 mm receivers. Again, standard calibration and imaging procedures were used in MIRIAD. The flux density scale was determined from scans on the planet Uranus and confirmed using the point-like source PKS 1921−293, the flux density of which had been measured four days prior to our observing run as 8.8 ± 0.9 Jy at 93.5 GHz. We detected a single point-like component in the 93.5 GHz image of PKS 1421−490 coincident with region A, the flux density of which we regard as being the total source flux density at this frequency, since the resolution of the shortest baseline is larger than the source. The upper limit on flux density at 93.5 GHz for region B and C is 5 mJy (5σ).

Errors in the flux densities reported in Table 1 are dominated by uncertainties in the primary flux calibration which are estimated to be of order ∼2% at cm wavelengths, and of order ∼10% at 3 mm.

2.4. Constraints on the Hotspot Radio Spectrum from ATCA Images

The hot spot is unresolved in the ATCA images, and is blended with emission from the surrounding regions. We are therefore unable to directly measure the flux density of the hot spot from the ATCA data. However, we are able to constrain the flux density of the hot spot, and we now discuss the methods used to obtain the upper and lower limits.

Using radio data that were first presented in Gelbord et al. (2005), we find upper limits on the hotspot flux density at 17.7 GHz and 20.2 GHz by summing the CLEAN components at the position of the hot spot. Similarly, we obtain an upper limit to the hotspot flux density at 93.5 GHz from the measurement

of total source flux density at that frequency. We obtain a lower limit on the hotspot flux density at 93.5 GHz via the following steps.

1. We subtract the LBA-measured hotspot flux density from the total source flux density at 2.3 GHz and 8.4 GHz to obtain two estimates of the nonhotspot flux density, from which we calculate a nonhotspot spectral index ($\alpha_{2.3\,\mathrm{GHz}}^{8.4\,\mathrm{GHz}}$(nonhotspot) = 0.78).

2. We extrapolate the nonhotspot power law to 93.5 GHz.

3. We reasonably assume that the nonhotspot spectrum becomes steeper toward higher frequencies. Therefore, the extrapolated flux density from step 2 is an upper limit to the nonhotspot flux density.

4. We subtract the nonhotspot upper limit from the observed entire source flux density to obtain a lower limit on the hotspot flux density at 93.5 GHz.

The assumption in step 3 is based on the observation that the nonhotspot emission arises in the lobes, jets, and the southern hot spot (the core is negligible). Jets and lobe spectra are often observed to steepen toward higher frequencies. Indeed, the 17.7 GHz and 20.2 GHz ATCA images indicate that the spectral index of the northern lobe region steepens significantly at higher frequency. The limits on hotspot flux density obtained from the ATCA images are represented by the tips of the arrows in Figure 2 and are listed in Table 1.

2.5. Optical Spectroscopy

Optical spectra were taken with the Magellan IMACS camera on 2005 May 14 in service mode. Three 10 minutes exposures were obtained using a long slit (0″.9 width) aligned with regions A and B. The 300 lines mm^{-1} grism was used to yield a spectral resolution of $R \sim 1000$ spanning roughly 4000–10000 Å. The spectra were reduced with IRAF. No standard stars were observed, so no effort was made to flux calibrate the spectra or to remove telluric absorption features.

No significant spectral features were detected in the spectrum of region A, consistent with synchrotron emission from a hot spot. However, only a very high equivalent width emission line could have been detected due to the low signal-to-noise ratio of these data.

The spectrum of region B contains several broad- and narrow-emission lines, which allowed a precise determination of the
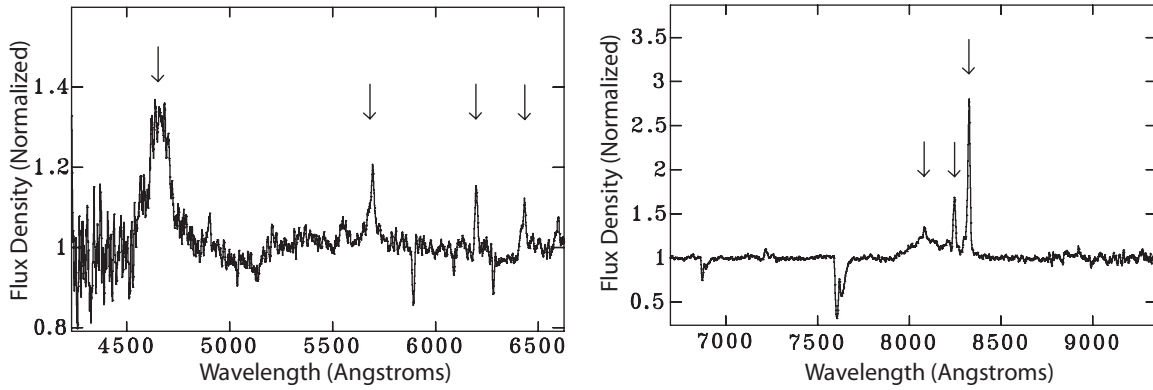
Figure 4. Normalized optical spectrum of region B. This spectrum clearly shows that region B is a broadline AGN at redshift 0.6628. Increasing in wavelength, the arrows indicate the positions of the following emission lines: Mg II 2799, [Ne v] 3426, [O II] 3726/3729, [Ne III] 3869, Hβ, [O III] 4959, [O III] 5007.

redshift (see Section 3.1). This is not the first spectrum of the nucleus to be published—a spectrum of region B was presented in G05. However, the spectrum presented in G05 did not allow identification of any spectral lines, because the strongest spectral features fell beyond the wavelength coverage, and the spectrum was taken as a single short exposure with a high background due to the predawn sky.

3. REGION B: THE ACTIVE GALACTIC NUCLEUS

3.1. Optical Spectrum of Region B

The normalized optical spectrum of region B is displayed in Figure 4. We detect several broad- and narrow-emission lines: Mg II 2799, [Ne v] 3346, and 3426, the blended [O II] 3726, 3729 doublet, [Ne III] 3869 and 3967, Hδ (marginal), Hγ, [O III] 4363, Hβ, and [O III] 4959 and 5007. Hβ has both a broad and narrow component; their measured FWHM values (uncorrected for instrumental resolution) are 6500 km s^{-1} and 516 km s^{-1}, respectively. The narrow Hβ line width is consistent with that of the O III lines (510 km s^{-1}). From these features we measure the redshift $z = 0.6628 \pm 0.0001$.

3.2. Spectral Energy Distribution of the Core

We did not detect the AGN with the LBA, but obtain an upper limit on the flux density of ∼8 mJy at 2.3 GHz. This is consistent with the ATCA core flux density measurements (see Table 1). The core is completely dominated by its optical emission. In fact, the optical flux density is so great relative to the radio ($\alpha_{8.6\,GHz}^{662.4\,nm} = 0.23 \pm 0.02$), the core would be classified as radio quiet in the strictest sense. The radio to optical spectral index cannot be explained in terms of standard synchrotron self-absorption models for flat radio spectra (e.g., Marscher 1988), since this would require at least part of the jet to be self-absorbed at optical wavelengths and would imply an unrealistically high magnetic field strength. This region has an optical spectral index $\alpha_o = 0.2 \pm 0.1$, in the range typical of quasars (Francis et al. 1991), suggesting that the strong optical emission may be due to an unusually large contribution from the accretion disk thermal component. The radio to X-ray spectral index ($\alpha_{8.6\,GHz}^{1\,keV} = 0.710 \pm 0.005$) is typical of radio galaxies at similar redshift (e.g., Belsole et al. 2006). The optical to X-ray spectral index is $\alpha_{ox} = 1.62$ (G05). There is clearly an excess of optical flux relative to the radio and X-ray flux when compared to samples of other radio galaxies (e.g., Gambill et al. 2003). Note that measurements of the *B*-band magnitude have shown no variability, to within 0.6 mag, over the past 35 years (GO5).

4. THE NORTHERN HOTSPOT

4.1. Morphology

Figure 3 shows the LBA image of the northern hot spot at 2.3 GHz. Less than 0.2 Jy (5% of the hotspot flux density) remains on the longest baseline (∼12.9 Mλ), implying that there is a little structure on scales smaller than 15 mas (100 pc). This limit on substructure within the hot spot is relevant to possible synchrotron self-absorption models for the hotspot spectrum, which we discuss further in Section 4.2.

The flux density of the hot spot in our LBA image is 60 % of the total source flux density at 2.3 GHz and 75 % at 8 GHz. The peak surface brightness is $I_{2.3\,GHz}^{peak} = 2600$ Jy arcsec^{-2}. Extrapolating to 8 GHz assuming $I_\nu \propto \nu^{-0.2}$ (the spectral index of $\alpha \sim 0.2$ between these frequencies is calculated in Section 4.2) and accounting for cosmological dimming and redshifting, we find that the peak surface brightness of the northern hot spot of PKS 1421−490 would be more than 1000 times brighter than the brightest hot spot of Cygnus A if they were at the same redshift (Carilli et al. 1999). The monochromatic hotspot luminosity is $L_{2.3\,GHz} = 8 \times 10^{27}$ WHz^{-1}.

A protrusion on the eastern edge of the hot spot resembles the "compact protrusions" seen in numerical simulations (e.g., Norman 1996). According to Norman (1996), a compact protrusion is produced in their three-dimensional nonrelativistic hydrodynamic simulations when the light, supersonic jet reaches the leading contact discontinuity. At this point, the jet is generally flattened to a width substantially less than the inlet jet diameter, and the compact protrusion arises where the jet impinges on the contact discontinuity surface.

The width of the hot spot at the peak (region HS1) is 400 pc measured perpendicular to the inferred jet direction. The lower surface brightness emission behind the hotspot peak (region HS2) is 700 pc measured perpendicular to the jet direction. The length of the hot spot (regions HS1 and HS2) is ∼1 kpc. The geometric mean of the major and minor axes is 0.63 kpc. This is a factor of 4 below the median value (2.4 kpc) of hot spot sizes given in Hardcastle et al. (1998). However, the size of the hot spot relative to the linear size of the source is consistent with the correlation between these parameters given in Hardcastle et al. (1998) and Jeyakumar & Saikia (2000).

The jet exhibits a bend of almost 60° (projected) ∼5 arcsec (35 kpc) from the core at the western end of the ridge of emission extending west from the hot spot in Figure 1. Bridle et al. (1994) showed that hotspot brightness is anticorrelated with the

apparent jet-deflection angle. They found that, for the 12 quasars in their sample, the ratio of hotspot flux density to lobe flux density decreases with larger jet bending angles, particularly when the deflection occurs abruptly. PKS 1421−490 does not follow this trend.

We detect what appears to be a jet knot (region J1) 512 mas (∼3.5 kpc projected) at a position angle −107° (north through east) from the hotspot peak. The knot is extended along a position angle almost perpendicular to the apparent jet direction. The major axis of the knot is poorly constrained due to the low signal to noise of this component, but the data suggest a width of ∼400–600 pc.

4.1.1. Interpretation of Region HS2

We now consider the interpretation of the lower surface brightness region HS2 just behind the hotspot peak. As mentioned above, the diameter of region HS2 perpendicular to the jet direction (700 pc) is much larger than the diameter of region HS1 (400 pc). The surface brightness of region HS2 is more than a factor of 10 times the peak surface brightness of the brightest hot spot of Cygnus A. In addition, the flux density from region HS2 alone (∼0.6 Jy at 2.3 GHz) is more than 4 times the total flux density of the whole counter lobe and hot spot. There are two possible interpretations for region HS2, and the interpretation of this region has implications for the interpretation of region HS1.

The first interpretation is in terms of emission from turbulent back-flow in the cocoon. If this interpretation is correct, we cannot appeal to Doppler beaming to account for the high surface brightness of region HS2 relative to other hotspots, and the high flux density relative to the counter hot spot and lobe. If we cannot appeal to Doppler beaming for region HS2, it would seem unreasonable to appeal to Doppler beaming to explain the high surface brightness of region HS1. The arm length symmetry places a tight upper limit on the expansion velocity of the lobes at $v_{\text{expansion}} < 0.1c$, indicating that the whole complex (region HS1 and HS2) cannot be advancing relativistically.

The second possible interpretation for region HS2 is that the emission is associated with oblique shocks in the jet as it approaches the hot spot. In this case, we may appeal to Doppler beaming to explain the high surface brightness of both regions HS1 and HS2. However, this interpretation would imply that the jet diameter at HS2 (∼700 pc) is significantly greater than the diameter of the hot spot at HS1 (∼400 pc) and also greater than the jet diameter at J1 (∼ 400–600 pc). It should be noted that the width of region J1, presumably associated with a jet knot, is poorly constrained due to the low signal to noise of this component. Future LBA observations at 1.4 GHz may provide better constraints on the size of regions J1 and HS2.

4.2. Modeling the Hotspot Spectral Energy Distribution

4.2.1. Low-Frequency Flattening

Figure 5 illustrates that the hotspot radio spectrum changes slope at GHz frequencies, becoming flatter toward lower frequencies. We now discuss this feature in more detail and consider the possible causes.

The hotspot spectral index calculated from our LBA flux density measurements is relatively flat at GHz frequencies ($\alpha_{2.3\,\text{GHz}}^{8.4\,\text{GHz}} = 0.22_{-0.05}^{+0.08}$). The hotspot spectrum cannot continue with this slope to millimeter wavelengths, since it would substantially overpredict the observed 93.5 GHz flux density. We
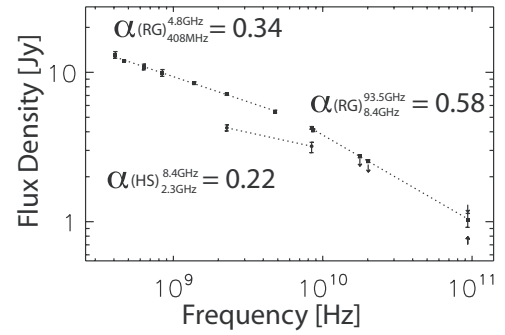

Figure 5. Radio spectrum of the entire radio galaxy (filled squares) and hot spot (filled circles and tips of arrows). This figure serves to illustrate the low-frequency flattening in the hotspot radio spectrum referred to in text (Sections 4.2.1 and 8). The dotted lines illustrate power-law fits to specific sections of the data.

therefore require that the hotspot spectrum be steeper at frequencies above 8 GHz, with spectral index $\alpha \gtrsim \alpha_{\text{LBA 8.4\,GHz}}^{\text{ATCA 93.5\,GHz}} = 0.48$.

Our conclusion of a flat spectral index at GHz frequencies based on the LBA flux density measurements is strengthened by inspection of the whole source spectrum (see Figure 5). The flux density of the entire radio galaxy has a spectral index of 0.58 above 8.4 GHz, but flattens to a spectral index of 0.34 below 4.8 GHz. The northern hot spot is the dominant component at GHz frequencies; hence, the flattening of the total source spectrum implies that there is flattening in the hotspot spectrum. There are a number of possible causes of this GHz frequency flattening, but most of them are implausible. We now consider a number of such explanations.

If synchrotron self-absorption were responsible for the flattening, the required magnetic field strength is $B_G \sim 10^{-5} \nu_p^5 \theta^4 F_p^{-2} (1+z)^{-1}$, where B_G is the magnetic field strength in Gauss, F_p is the peak flux density in Jy, ν_p is the frequency in GHz at the peak, and θ is the angular size in milliarcseconds (de Young 2002, p. 325). In the case of the northern hot spot of PKS 1421−490 we estimate (conservatively) $\nu_p \sim 1$ GHz, $\theta \sim 100$ mas, $F_p \sim 5$ Jy and $z = 0.663$. Therefore, a magnetic field strength of $B \sim 20$ G is required to produce the observed flattening—four orders of magnitude greater than the equipartition magnetic field strength. Less than 0.2 Jy (5% of the hotspot flux density) remains on the longest baselines (12.9 Mλ ⇒ 15 mas resolution), implying that the hot spot cannot be composed of many small self-absorbed subcomponents. Therefore, we do not consider synchrotron self-absorption to be a viable explanation for the flattening.

We next consider free–free absorption by interstellar clouds in the hotspot environment as a possible mechanism for the observed flattening of the radio spectrum. Consider a cloud of size L_{kpc} kpc, temperature $T_4 \times 10^4$ K, electron number density n_e cm^{-3} and pressure $p_{-12} \times 10^{-12}$ dyn cm^{-2}. The optical depth τ to free–free absorption at a frequency ν_{GHz} GHz is given by (e.g., de Young 2002, p. 326)

$$\tau = 3.3 \times 10^{-4} n_e^2 L_{\text{kpc}} \nu_{\text{GHz}}^{-2.1} T_4^{-1.35} \tag{1}$$

$$= 2 \times 10^{-4} L_{\text{kpc}} \nu_{\text{GHz}}^{-2.1} p_{-12}^2 \left(\frac{n_e}{n}\right)^2 T_4^{-3.35}. \tag{2}$$

Assuming a characteristic pressure in the outer regions of an elliptical galaxy $p \sim 10^{-12}$ dyn cm^{-2}, a characteristic temperature for an ionized cloud $T \sim 10^4$ K and a reasonable

cloud size $L \lesssim 1$ kpc, the optical depth to free–free absorption above 1 GHz is less than 5×10^{-5}.

We therefore interpret the change of slope in the hotspot radio spectrum in terms of a change in the underlying electron energy distribution. In Section 4.2.4, we model the spectral energy distribution (SED) by incorporating a low-energy cutoff in the electron energy distribution. A low-energy cutoff at some minimum Lorentz factor $\gamma_{\min}$ produces a spectrum with $F_\nu \propto \nu^{1/3}$ at frequencies below the characteristic emission frequency of electrons with a Lorentz factor $\gamma_{\min}$ (see e.g., Worrall & Birkinshaw 2006). We must emphasize that an instantaneous cutoff in number density is not physical—it is merely an approximation to a sharp turnover in the electron energy distribution. In Section 8, we show that interpreting the observed flattening in terms of a turnover in the electron energy distribution has considerable implications.

Low-frequency flattening in hotspot spectra has been observed in a small number of other objects (see Section 1).

4.2.2. The High-Frequency Synchrotron Spectrum

The hotspot spectrum remains relatively flat between 8 GHz and 93.5 GHz, having a spectral index $0.4 < \alpha < 0.6$ (based on the two-point spectral index from the 8.4 GHz LBA data point to the ATCA upper and lower limits at 93.5 GHz). The synchrotron spectrum above 93 GHz is poorly constrained, but the simplest model—a power-law spectrum with a spectral index $0.4 < \alpha < 0.6$ and an exponential cutoff at high frequency (i.e., a synchrotron spectrum from a power-law electron energy distribution with number density set to zero above $\gamma_{\max}$) is unable to satisfy the optical data and the 2MASS infrared upper limits simultaneously. Either a break to a steeper spectrum somewhere between $\sim 10^{11}$–10^{13} Hz is required, or a gradual cutoff at high electron energy, rather than an abrupt cutoff at $\gamma_{\max}$ must exist. Given the high radio luminosity, hence high magnetic field strength, synchrotron losses are likely to be important. We therefore allow for a synchrotron-cooling break at an arbitrary break frequency in order to fit the radio through optical spectrum. Different choices of model spectrum are possible, but they would not significantly affect our major results. We discuss the model electron energy distribution in Section 4.2.4, and further discuss the self-consistency of this model in Section 6.

4.2.3. Hotspot X-ray Emission

Figure 6 shows the SED of the northern hot spot. The level of X-ray flux density relative to the optical flux density indicates the presence of two distinct spectral components: synchrotron emission from radio to optical frequencies, and inverse Compton emission at X-ray frequencies and above.

The energy density of the locally generated synchrotron emission within the hot spot (assuming no Doppler beaming) is more than 10^4 times the energy density of the CMB at this redshift. If the hotspot plasma is moving relativistically with velocity $v = \beta c$ at an angle θ to the line of sight, the ratio of synchrotron to CMB energy density is reduced by a factor of $\sim \Gamma^{-2}\delta^{-3}$, where $\delta = [\Gamma(1 - \beta \cos \theta)]^{-1}$ is the Doppler factor and $\Gamma = (1 - \beta^2)^{-1/2}$ is the bulk Lorentz factor, and we have assumed the hot spot is associated with plasma moving through a stationary volume/pattern rather than a moving blob, so that $I_\nu = \delta^2 I'_{\nu'}$ (Lind & Blandford 1985). Therefore, if $\delta \lesssim 6$ (assuming $\Gamma \sim \delta$), inverse Compton scattering of locally generated synchrotron photons is the dominant source of inverse Compton X-ray emission. While a Lorentz factor of $\Gamma \sim 6$ is not
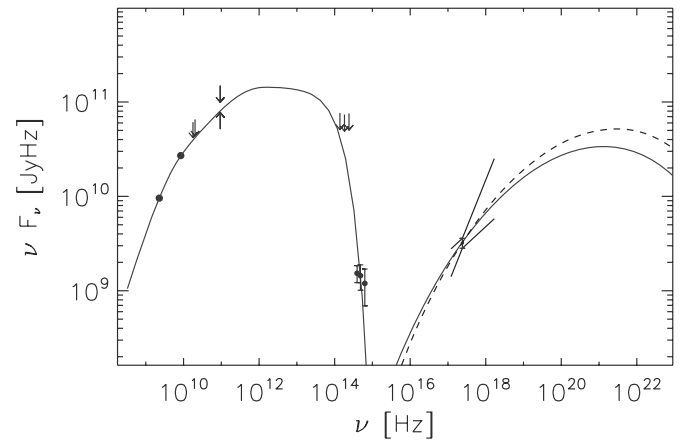

Figure 6. Hotspot SED with SSC model overlaid. The "bow-tie" around the X-ray data point indicates the 1σ range of X-ray slopes. The solid line is the best-fit synchrotron plus self-Compton model spectrum with the Doppler factor fixed at $\delta = 1$. The dashed line is the best-fit SSC component with the Doppler factor fixed at $\delta = 3$. The model synchrotron spectra for $\delta = 3$ and $\delta = 1$ are exactly the same, and so do not appear as separate curves in the plot. The LBA data points (plotted as filled circles) have error bars smaller than the symbol size. Tips of arrows mark the position of upper and lower limits. X-ray, optical and infrared points are taken from Gelbord et al. (2005).

ruled out, such a high Lorentz factor is not required by the data, and we consider only Lorentz factors $\Gamma \lesssim 3$. We therefore ignore the inverse Compton scattering of CMB photons in the following treatment. We also ignore any contribution to the X-ray flux density from "upstream Compton" scattering (Georganopoulos & Kazanas 2003), whereby electrons in the jet upstream from the hotspot inverse Compton scatter synchrotron photons produced within the hot spot. We note that if the upstream Compton process makes a significant contribution to the observed X-ray flux density, the SSC flux density must be less than the observed flux density in which case the magnetic field strength in the hot spot would be greater than that reported in Table 2, and therefore greater than the equipartition value.

4.2.4. Synchrotron Self-Compton Modeling

To model the radio to X-ray spectral energy distribution, we use the standard one-zone SSC model: a spherical region of plasma with uniform density and magnetic field strength. We assume that the magnetic field is "tangled" with an isotropic distribution of field direction. We further assume that the number density of electrons per unit Lorentz factor is described by

$$\bar{N}(\gamma) = \begin{cases} 0 & \gamma < \gamma_{\min}, \quad \gamma > \gamma_{\max} \\ \frac{K_e \gamma_b}{(a-1)} \gamma^{-(a+1)} g\left(\frac{\gamma}{\gamma_b}\right) & \gamma_{\min} < \gamma < \gamma_{\max} \end{cases} \quad (3)$$

where

$$g\left(\frac{\gamma}{\gamma_b}\right) = \begin{cases} 1 - \left(1 - \frac{\gamma}{\gamma_b}\right)^{a-1} & \gamma < \gamma_b \\ 1 & \gamma > \gamma_b. \end{cases} \quad (4)$$

Here, $\bar{N}(\gamma)$ is the volume-averaged energy distribution produced by continuous injection of a power-law energy distribution $N(\gamma) = K_e \gamma^{-a}$ at a shock with synchrotron cooling in a uniform magnetic field downstream. It describes a broken power-law spectrum with the electron spectral index smoothly changing from $-a$ to $-(a + 1)$ at $\gamma \approx \gamma_b$. The break in the electron spectrum at γ_b corresponds to the electron energy at which the synchrotron-cooling timescale is comparable to the

Table 2
SSC Model Parameters for Northern Hotspot

Fixed Parameters					Derived Parameters						
δ	R (pc)	α	ν_b (Hz)	ν_{max} (Hz)	B (mG)	B/B_{eq}	n_e ($\times 10^{-5}$ cm^{-3})	γ_{min}	γ_b ($\times 10^4$)	γ_{max} ($\times 10^5$)	$\alpha_{0.5\,keV}^{7.0\,keV}$
1.0	320	0.53	5×10^{11}	10^{14}	3.2 ± 0.5	$1.5^{+0.3}_{-0.2}$	2.7 ± 0.4	650 ± 80	$\gtrsim 0.8$	1.1 ± 0.1	0.5 ± 0.1
2.0	320	0.53	5×10^{11}	10^{14}	1.0 ± 0.2	0.75 ± 0.15	2.2 ± 0.3	800 ± 100	$\gtrsim 1$	1.4 ± 0.2	0.45 ± 0.1
3.0	320	0.53	5×10^{11}	10^{14}	0.5 ± 0.1	0.5 ± 0.1	1.9 ± 0.3	950 ± 100	$\gtrsim 1.1$	1.6 ± 0.2	0.45 ± 0.1

Notes. The quoted uncertainties on model parameters are an estimate of the level of uncertainty from model fitting, and correspond to the range of parameter values in the set of models having $\chi^2 < \chi^2_{min} + 2.71$.

dynamical timescale for electrons to escape from the hot spot. The synchrotron-cooling break is discussed further in Section 6.

For the electron energy distribution described by $\bar{N}(\gamma)$, and given a particular radius, redshift, Doppler factor, and spectral index, the synchrotron plus self-Compton spectrum is characterized by the five parameters $K_e, B, \gamma_{min}, \gamma_b, \gamma_{max}$. In calculating the model spectrum, these parameters appear in the following combinations (see Appendix A):

$$A_{syn} = K_e \Omega_0^{\alpha+1} \quad (5)$$

$$A_{ssc} = K_e \gamma_b \quad (6)$$

$$\nu_1 = \frac{\delta}{(1+z)} \frac{3}{4\pi} \Omega_0 \gamma_{min}^2 \quad (7)$$

$$\nu_b = \frac{\delta}{(1+z)} \frac{3}{4\pi} \Omega_0 \gamma_b^2 \quad (8)$$

$$\nu_2 = \frac{\delta}{(1+z)} \frac{3}{4\pi} \Omega_0 \gamma_{max}^2, \quad (9)$$

where $\alpha = (a-1)/2$ is the radio spectral index between frequencies ν_1 and ν_b, Ω_0 is the nonrelativistic gyrofrequency. The parameters ν_1, ν_b, and ν_2 correspond to the characteristic frequency emitted by electrons with the Lorentz factor γ_{min}, γ_b, and γ_{max} in a magnetic field of flux density B, and are therefore identified with the low-frequency turnover, synchrotron-cooling break, and high-frequency cutoff, respectively. The advantage of this formulation, described in the Appendix, is that it allows the model to be specified in terms of the observed values of ν_1, ν_b, and ν_2. The parameters A_{syn} and A_{ssc} are normalization factors for the synchrotron and SSC spectral components respectively.

We estimate best-fit values for B, K_e, γ_{min}, γ_b, and γ_{max} using chi-squared minimization with the following three constraints. (1) We fix the electron energy index at $a = 2.06$, so that the spectral index $\alpha = 0.53$ for frequencies $\nu_1 \ll \nu \ll \nu_b$ (that is between about 10 GHz and 100 GHz). This is the electron energy index determined from modeling the hotspot radio spectrum as described in Section 5. The spectral index $\alpha = 0.53$ also agrees with the ratio of peak surface brightness (at the location of the hot spot) in the 17.7 GHz and 20.2 GHz ATCA images. (2) We fix the radius at $R = 320$ pc. The radio hot spot is elongated in an approximately cylindrical shape of volume $V \approx 4 \times 10^{57}$ m^3. A radius of 320 pc gives a spherical model of equal volume. (3) We fix the break frequency at $\nu_b = 500$ GHz. This is close to the lowest break frequency allowed by the data. Higher break frequencies are permitted but cause a worse fit to the optical data. The break frequency is not well constrained by the data, but the results are not sensitive to the assumed value of the break

frequency. (4) We fix the upper cutoff frequency at $\nu_{max} = 10^{14}$ Hz to fit the optical flux densities.

We determined best-fit parameter values while fixing the Doppler factor at $\delta = 1, 2$ and 3. The derived model parameters are presented in Table 2. The uncertainties in Table 2 are determined from the range of parameter values in the set of models having $\chi^2 < \chi^2_{min} + 2.71$. The observed X-ray spectral index was not included in the chi-squared calculations, but the model X-ray spectral index is consistent with the observed value within the uncertainties.

In Figure 6 we plot the observed hotspot flux densities with the best-fit model spectra (for Doppler factors fixed at $\delta = 1$ and $\delta = 3$) overlaid. The simple one-zone model with a near equipartition magnetic field strength provides a good description of the available data. Hardcastle et al. (2002) used more complicated spectral and spatial models for three sources, and found that this did not have a significant effect on the derived plasma parameters. We are therefore confident in our parameter estimates using this "first-order" one-zone model.

5. MODELING THE RADIO SPECTRUM OF THE ENTIRE RADIO GALAXY

We now describe a consistency check for the model of the hotspot radio spectrum in terms of a cutoff in the electron energy distribution at γ_{min}. This check is based on the observed flattening in the spectrum of the entire radio galaxy (Figure 7). In order to test whether the observed flattening is consistent with the inferred low-energy cutoff in the electron distribution, we fit a simple two-component model to the radio galaxy spectrum between 408 MHz and 93.5 GHz. The model components are: (1) The synchrotron spectrum produced by the electron energy distribution of Equation (3). This component describes emission from the hot spot. (2) A pure power-law approximating emission from the rest of the source. Note that the core flux density is negligible compared with that of the jets, lobes and hotspots, so that no component is included to represent emission from the AGN.

The synchrotron spectrum of component 1 is calculated using equation (A7). We assume the same source volume as in Section 4.2.4, fix the lab frame break frequency at $\nu_b = 500$ GHz and the lab frame high-frequency cutoff at $\nu_2 = 1.1 \times 10^{14}$ Hz, consistent with the values determined from modeling the hotspot spectrum in Section 4.2.4. With these assumed values, the parameters ν_b and ν_2 do not affect the shape of the spectrum below about 100 GHz, but they weakly affect the calculation of equipartition magnetic field strength. The spectrum of component 1 is therefore determined by the spectral index α_1, the turnover frequency ν_1 and the synchrotron amplitude $A_{syn} = K_e \Omega_0^{\alpha_1+1}$. The flux density of the second
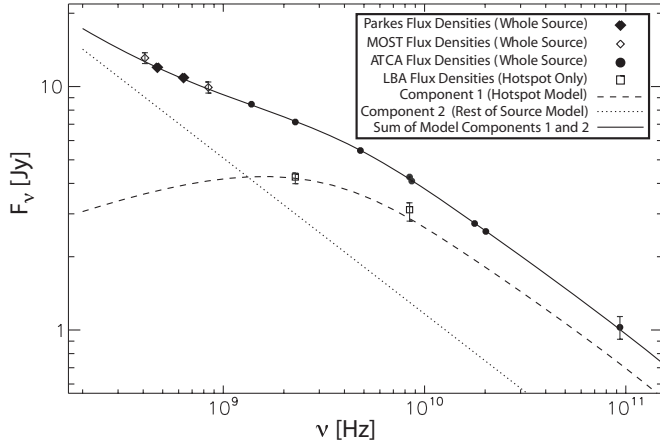
Figure 7. Radio spectrum of the radio galaxy PKS 1421−490. Open diamonds represent flux densities of the entire radio galaxy from the Molonglo Synthesis Radio Telescope (MOST). Filled diamonds represent flux densities of the entire radio galaxy from the Parkes telescope. Filled circles represent flux densities of the entire radio galaxy from the ATCA. Open squares represent flux densities of the Northern hot spot from the LBA (see Table 1). Also shown is the spectral decomposition described in Section 5. Component 1 (curved dashed line) is the angle-averaged synchrotron spectrum from a power-law electron distribution of the form $N(\gamma) \propto \gamma^{-2.06}$ with a low-energy cutoff at a Lorentz factor corresponding to $\nu_1 = 2.6$ GHz (see Equation (7)). This component describes emission from the hot spot, and is consistent with the LBA flux densities plotted as open squares. Component 2 (straight dotted line) is a pure power-law with spectral index 0.64. This component is an approximation to the emission from the rest of the source. The solid line is the sum of components 1 and 2. Model parameters are given in Table 3.

component is of the form

$$F_{\nu,2} = F_{2.3\,\text{GHz},2} \left(\frac{\nu}{2.3\,\text{GHz}} \right)^{-\alpha_2} \quad (10)$$

Chi-squared minimization was used to determine the best-fit values for the parameters α_1, A_{syn}, ν_{min}, $F_{2.3\,\text{GHz},2}$ and α_2. The resulting model is shown in Figure 7. This simple two-component model provides an excellent fit to the radio galaxy spectrum. Component 1 (describing emission from the hot spot) is in good agreement with the LBA flux density measurements at 2.3 GHz and 8.4 GHz. We emphasize that the LBA flux density measurements were not included in the fitting process, but are included in Figure 7 for comparison with the spectrum of component 1.

Again, we point out that the cutoff in the number density per unit Lorentz factor below γ_{min} used in our modeling is not physically realistic, it is merely an approximation to an electron energy distribution with a sharp turnover. The success of this simple model in simultaneously accounting for the flattening in both the hotspot spectrum and the radio galaxy spectrum supports an interpretation of the flattening in terms of a sharp turnover in the hotspot electron energy distribution at a Lorentz factor of order $\gamma \sim 600$.

6. SYNCHROTRON COOLING BREAK

The magnetic field strength inferred from spectral modeling in Section 4.2.4 implies that there should be a synchrotron-cooling break in the hotspot radio spectrum at ~ 1 GHz if the electron energy distribution injected at the shock is a pure power law. This is inconsistent with the lower limit on the break frequency estimated from spectral modeling, $\nu_b \gtrsim 500$ GHz. In this section we consider the production of the cooling break, and possible reasons for the inconsistency.

Table 3
Model Parameters from Fitting the Radio Spectrum of the Entire Radio Galaxy

Component 1 (Hotspot)					Component 2	
$F(2.3\,\text{GHz})$	α	ν_1	B_{eq}	$\gamma_{\text{min}}^{\text{eq}}$	$F(2.3\,\text{GHz})$	α
(Jy)		(GHz)	(Gauss)		(Jy)	
4.15 ± 0.6	$0.53^{+0.1}_{-0.3}$	$2.6^{+0.3}_{-0.5}$	$2.05^{+0.35}_{-0.1} \times 10^{-3}$	550^{+50}_{-100}	3.0 ± 0.6	0.65 ± 0.1

Notes. The quoted uncertainties on model parameters are an estimate of the level of uncertainty from modelfitting, and correspond to the range of parameter values in the set of models having $\chi^2 < \chi^2_{\text{min}} + 2.71$.

The standard continuous injection hotspot model (Heavens & Meisenheimer 1987) predicts that the radio spectrum will steepen from α_{in} to $\alpha_{\text{in}} + 0.5$ at a frequency, ν_b, corresponding to the electron energy at which the synchrotron-cooling timescale τ_{cool} is equal to the dynamical timescale τ_{esc} for electrons to escape the hot spot. The break frequency is an important constraint on the physics of the hot spot. In general, it depends on the magnetic field strength, hotspot radius, outflow velocity, Doppler factor and the presence or absence of a re-acceleration mechanism within the hot spot. We consider a model in which the escape timescale τ_{esc} is the time taken for the flow to cross the hot spot and the cooling timescale is the synchrotron half-life. Let R be the hotspot radius, $v = \beta_f c$ the flow velocity within the hot spot (note that this is not the same as the advance velocity of the hot spot), δ_f the corresponding Doppler factor of the flow within the hot spot, and U_B the magnetic field energy density ($U_B = B^2/2\mu_0$ in SI units, $U_B = B^2/8\pi$ in cgs units).

$$\tau_{\text{esc}} = \frac{2R}{\beta_f c} \quad (11)$$

$$\tau_{\text{cool}} = \frac{\gamma}{|d\gamma/dt|} \quad (12)$$

$$= \frac{3m_e c}{4\sigma_T U_B \gamma} \quad (13)$$

Equating the two timescales and combining with Equation (8) for the break frequency in terms of the break Lorentz factor, we obtain the following expression for the break frequency

$$\nu_b \approx 60 \frac{\delta_f^{\frac{7+4\alpha}{\alpha+1}} \beta_f^2}{(1+z)} \left(\frac{B_{\delta_f=1}}{\text{mG}} \right)^{-3} \left(\frac{R}{\text{kpc}} \right)^{-2} \text{GHz} \quad (14)$$

$$= 60 \frac{\delta_f^6 \beta_f^2}{(1+z)} \left(\frac{B_{\delta_f=1}}{\text{mG}} \right)^{-3} \left(\frac{R}{\text{kpc}} \right)^{-2} \text{GHz} \quad (\alpha = 0.5) \quad (15)$$

where $B_{\delta_f=1}$ is the magnetic field strength derived from SSC modeling under the assumption $\delta_f = 1$. For a Doppler factor $\delta_f = [\Gamma(1 - \beta_f \cos\theta)]^{-1}$, the magnetic field strength estimated from SSC modeling is reduced by a factor of approximately $\delta_f^{-\frac{\alpha+2}{\alpha+1}}$ (e.g., Worrall & Birkinshaw 2006). Equation (15) exhibits a strong dependence on the Doppler factor because of the strong dependence of the break frequency on the magnetic field strength.

Let us first consider the production of the cooling break in a hot spot associated with a strong relativistic normal shock in which the postshock velocity $\beta_f \approx 0.3$, $\delta_f \approx 1$, redshift $z = 0.663$, magnetic field $B = 3$ mG (as determined from SSC modeling in Section 4.2.4) and radius $R = 0.3$ kpc (half the geometric mean of the longest and shortest angular sizes of the

2.3 GHz LBA image). For such a model, the predicted break frequency is $\nu_b \approx 1$ GHz. This is inconsistent with the lower limit from spectral modeling, $\nu_b \gtrsim 500$ GHz. Moreover, the break frequency estimated from spectral modeling is inconsistent with the proposed correlation between break frequency and equipartition magnetic field strength (e.g., Brunetti et al. 2003; Cheung et al. 2005) which also predicts a break frequency $\nu_b \sim 1$ GHz. The discrepancy between predicted break frequency and the observed lower limit would be alleviated if the magnetic field strength were $\lesssim 0.15$ of the value estimated from SSC modeling. However, if this were the case, the model SSC spectrum would overpredict the observed X-ray flux density.

Let us now consider the effect of Doppler beaming on the observed break frequency as a possible means of resolving this difficulty. Assuming a postshock flow velocity $\beta_f^2 \sim (1 - \delta_f^{-2})$ and a spectral index of $\alpha \sim 0.5$, a moderate Doppler factor $\delta_f \gtrsim 1.9$ is sufficient to increase the predicted break frequency above 500 GHz, while maintaining agreement between the SSC model spectrum and the observed flux densities.

There is also the possibility that distributed re-acceleration within the hot spot is affecting the production of the cooling break. Meisenheimer et al. (1997) have suggested that distributed re-acceleration is required to explain the spectra of the so-called low-loss hotspots. These are hotspots whose spectra are characterized by a power-law with $\alpha \approx 0.6-0.8$ that extends to high frequency ($\nu > 10^{12}$ Hz) without the predicted break in the spectrum. Distributed re-acceleration has also been proposed to explain the diffuse infrared/optical emission observed around some hotspots (Prieto et al. 2002; Roeser & Meisenheimer 1987; Meisenheimer 2003), as well as the variation in the X-ray spectral index around the hotspots of Cygnus A (Bałucińska-Church et al. 2005), and the existence of flat radio spectrum regions distributed over much of the hotspot area in Cygnus A (Carilli et al. 1999). The favored mechanism for re-acceleration is stochastic (second order Fermi) acceleration via magnetohydrodynamic turbulence (Meisenheimer et al. 1997; Prieto et al. 2002; Bałucińska-Church et al. 2005).

Lastly, it is possible that there is more than one site of particle injection, or that the hot spot is not in a steady state.

7. IS DOPPLER BEAMING SIGNIFICANT IN THE NORTHERN HOTSPOT OF PKS 1421−490?

The aim of this section is to assess the likelihood that emission from the northern hot spot of PKS 1421−490 is Doppler beamed. To do so, in Section 7.1 we lay out the evidence for Doppler beaming in the northern hot spot, then discuss results of numerical simulations and radio studies that indicate Doppler beaming may be significant in hotspots of radio galaxies and quasars. In Section 7.2 we consider the angle to the line of sight of PKS 1421−490, which should be small if Doppler beaming is to be important. In Section 7.3 we estimate the magnitude of the Doppler factor that would be required to account for various properties of the hot spot. In Section 7.4 we discuss two possible arguments against Doppler beaming.

7.1. Arguments for Doppler Beaming

The northern hot spot of PKS 1421−490 is extremely luminous at both radio and X-ray wavelengths. The X-ray luminosity between 2 and 10 keV, $L_{2-10\,\mathrm{keV}} = 3 \times 10^{44}$ ergs s^{-1}, is comparable to the X-ray luminosity of the entire jet of PKS 0637−752, without relativistic corrections. The peak radio surface brightness is hundreds of times greater than that

of the brightest hot spot in Cygnus A (Carilli et al. 1999). Consequently, the equipartition magnetic field strength for a Doppler factor of unity is greater by a factor of $\sim 5-10$, and the minimum energy density is greater by a factor of ~ 50 than values typically evaluated for bright hotspots in other radio galaxies (Meisenheimer et al. 1997; Tavecchio et al. 2005; Kataoka & Stawarz 2005). The northern hot spot contributes 60% of the total source flux density at 2.3 GHz, and 75% at 8 GHz. Identifying the peak of region C in the ATCA image as the counter hot spot, we estimate the hot spot to counter hotspot flux density ratio to be $R_{\mathrm{hs}} \sim 300$ at 20 GHz. In the *Chandra* X-ray band, the counter-hotspot is undetected, and we conservatively estimate $R_{\mathrm{hs}} > 100$ at X-ray wavelengths. These are all indications that the hotspot emission may be Doppler beamed. Moreover, we have shown in Section 6 that Doppler beaming may account for the absence of a synchrotron-cooling break below 500 GHz. We now discuss the results of numerical simulations and radio studies that indicate Doppler beaming may be important in hotspots of radio galaxies.

Numerical simulations of supersonic jets in two and three dimensions (e.g., Aloy et al. 1999; Norman 1996; Komissarov & Falle 1996; Tregillis et al. 2001) suggest that flow speeds in and around hotspots can be much larger than those expected from the one-dimensional strong shock model, because the shock structure at the jet termination is more complex than a single terminal Mach disk. The simulated jets undergo violent structural and velocity changes near the jet head due to pressure variations in the turbulent cocoon. These violent changes in the jet affect the hotspot structure, and may result in an oblique shock (or shocks) near the hot spot (Aloy et al. 1999; Norman 1996). The postshock velocity of an oblique shock can be much higher than the postshock velocity of a normal shock if the angle between the flow velocity and the shock normal is close to the Mach angle. Therefore, the instantaneous flow velocity through the hot spot may be high enough to produce significant Doppler effects (Aloy et al. 1999).

If the terminal shock is not highly oblique, the postshock velocity may be relativistic if the jet contains a dynamically important magnetic field. The magnetic field can reduce the shock compression ratio and result in a higher postshock Lorentz factor than that in an unmagnetized shock (see e.g., Double et al. 2004). The postshock velocity in a magnetized shock depends on the angle between the magnetic field and the shock plane, the equation of state in the preshock and postshock plasma, and the magnetization parameter $\sigma = B^2/4\pi\rho c^2$ (Double et al. 2004). In the case where the magnetic field is perpendicular to the jet direction, significant postshock Lorentz factors ($\Gamma_2 \gtrsim 2$) can be achieved if $\sigma \gtrsim 3$, depending on the equation of state. We suggest that, given the high magnetic field strength in the northern hot spot of PKS 1421−490, magnetic cushioning of the terminal shock due to the presence of a strong magnetic field in the jet may be important.

In addition to the results of numerical simulations, observational evidence also indicates that Doppler beaming of hotspot emission may be significant. For example, the brighter and more compact hot spot is generally found on the side of the source with the brighter kpc-scale jet (e.g., Bridle et al. 1994; Hardcastle et al. 1998). This effect is more evident in samples of quasars than in samples including low power sources, which suggests that the observed correlation between hotspot brightness and jet brightness is related to Doppler beaming (Hardcastle et al. 1998). However, Hardcastle (2003) suggest that only moderate hotspot flow velocities ($\beta \sim 0.3$) are required to account for

this observed correlation. Dennett-Thorpe et al. (1997) found that regions of high surface brightness in the lobes of radio galaxies have flatter radio spectra on the side corresponding to the brighter jet. They suggest that Doppler shifting of a curved hotspot spectrum may produce such a correlation. Again, only moderate flow speeds of $\beta \lesssim 0.5$ are required to account for this correlation (Ishwara-Chandra & Saikia 2000). Georganopoulos & Kazanas (2003) have suggested that deceleration of a relativistic flow from $\Gamma \sim 3$ to $\Gamma \sim 1$ in hotspots can explain the wide range of observed hotspot SEDs as being purely an effect of source inclination. However, Hardcastle (2003) and Hardcastle et al. (2004) have contested this interpretation. Rather, they argue, the shape of the hotspot SED depends only on the hotspot radio luminosity.

7.2. Jet Inclination Angle

We now consider the angle to the line of sight for PKS 1421−490, if Doppler beaming is to be important.

The AGN of PKS 1421−490 exhibits broad emission lines (see Section 3.1). On the basis of the unified scheme for active galaxies, we therefore expect the angle to the line of sight to be less than $\sim 45°$ (Urry & Padovani 1995). Another indication of a small angle to the line of sight is the existence of a $60°$ bend in the northern jet, ~ 5 arcsec (35 kpc) from the AGN at the western end of the ridge of emission extending west from the hot spot in Figure 1. Such a large jet deflection is hard to understand if it is indicative of the true bending angle. The well known resolution to this problem is that the jet is viewed close to the line of sight, and the effect of projection causes a relatively small jet deflection to appear much larger than it actually is.

7.3. Estimates of the Doppler Factor

We now consider the magnitude of the Doppler factor that would be required to account for the various observed properties.

Let R_{hs} be the hot spot to counter hotspot flux density ratio, β_{hs} the bulk flow velocity in the hot spot divided by the speed of light, θ the jet angle to the line of sight, and α the spectral index. If the two hotspots of PKS 1421−490 are identical, and the difference in flux density is purely the result of relativistic beaming, then

$$\beta_{hs} \cos \theta = \frac{R_{hs}^{\frac{1}{2+\alpha}} - 1}{R_{hs}^{\frac{1}{2+\alpha}} + 1} \qquad (16)$$

(e.g., de Young 2002, p. 73).

The observed hot spot to counter-hotspot flux density ratio is $R_{hs} \sim 300$ at 20.2 GHz, hence: $\beta_{hs} \cos \theta \sim 0.81$, $\Gamma_{hs} > 1.7$, and $\theta < 36°$. A moderate Lorentz factor of $\Gamma_{hs} \gtrsim 1.7$ can account for the observed hotspot flux density ratio. The bend in the northern jet means that we cannot assume the same inclination angle for the jet and counter-jet, so Equation (16) does not strictly apply, but the above calculations serve to illustrate that the required Lorentz factor is not large. If the jet is angled close to the line of sight, the real difference in inclination angle between jet and counter-jet may not be large.

It should be noted that there is a difference between the times at which we see the two hotspots. In the case of PKS 1421−490 this difference is $\sim (3 \times 10^5 \tan \theta)$ yr, where θ is the angle to the line of sight. In Equation (16), there is an implicit assumption that the brightness of the hotspots remain constant over a timescale of $\sim 10^5$–10^6 years.

We summarize below the estimates of the Doppler factor required to account for various properties of the hot spot.
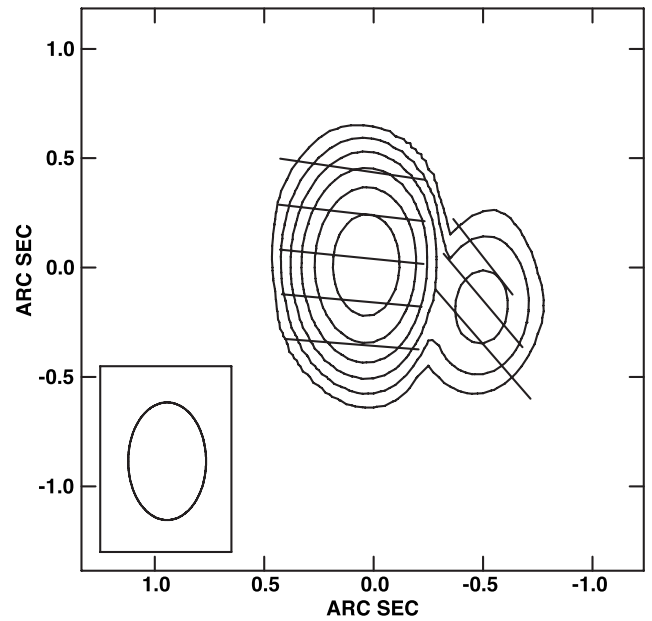

Figure 8. 20.16 GHz ATCA contours of polarized intensity with polarization E-vectors overlaid. The length of the polarization E-vectors is proportional to the fractional polarization, with 1 arcsecond corresponding to 15% fractional polarization. The polarization vectors have been rotated by $-1°.8$ to account for the observed rotation measure of ~ 140 rad m^{-2}. The main peak corresponds to the hot spot (regions HS1 and HS2), while the secondary peak is associated with region J1 in Figure 3, presumably associated with a jet knot. Both regions are $\sim 8\%$–10% polarized. The map peak is 0.19 Jy beam^{-1}. Contour levels: 3.5 mJy beam^{-1} × (1, 2, 4, 8, 16, 32, 64). Beam FWHM: 0.54 × 0.36 arcsec. The scale of this image is 7.0 kpc arcsecond^{-1}.

1. A bulk Lorentz factor $\Gamma \gtrsim 1.7$ is required to account for the observed hot spot to counter hotspot flux density ratio of $R_{hs} \sim 300$. If the bend in the northern jet is such that a decrease in inclination angle is produced, the required bulk Lorentz factor is lower.

2. A Doppler factor $\delta \gtrsim 1.9$ is required to account for the observed lower limit on the break frequency $\nu_b \gtrsim 500$ GHz (see Section 6).

3. A Doppler factor $\delta \sim 3$ is required to reduce the SSC model magnetic field strength to a value comparable to that calculated for other radio galaxies (~ 100–500 μG) (Kataoka & Stawarz 2005). However, such agreement is not essential since some variation in the radio galaxy population would be expected.

7.4. Arguments Against Doppler Beaming

In Section 4.1.1, we argued that the broad emission to the west of the hotspot peak (region HS2) may be associated with turbulent back-flow in the cocoon, and therefore cannot be Doppler beamed. As further discussed in Section 4.1.1, if the high surface brightness of region HS2 is not the result of Doppler beaming, then it seems unreasonable to argue that the high surface brightness of region HS1 is the result of Doppler beaming.

Another possible argument against Doppler beaming comes from interpreting the radio polarization. Figure 8 is a contour map of the linearly polarized intensity at 20 GHz in the vicinity of the hot spot, with the polarization position angle indicated by the vectors overlaid. The main peak in the contour map is associated with the hot spot (regions HS1 and HS2). The offset of the secondary peak relative to the main peak

places it at the same position as region J1 in Figure 3. The position angle of the **E**-vectors in the hot spot indicate that the magnetic field (perpendicular to the **E**-vectors) is aligned nearly perpendicular to the jet direction. The magnetic field direction is often identified with the shock plane, because the component of the magnetic field in the plane of the shock is amplified, while the component of magnetic field perpendicular to the shock plane is conserved. Figure 8 therefore indicates that the terminal shock is not highly oblique. If the terminal shock is not highly oblique the postshock velocity cannot be highly relativistic unless the magnetic field is dynamically important (see Section 7.1 and Double et al. 2004). If the magnetic field is dynamically important, this argument against Doppler beaming based on the polarization position angle is not valid.

8. INTERPRETING THE LOW-FREQUENCY FLATTENING IN THE RADIO SPECTRUM OF THE NORTHERN HOT SPOT

The aim of this section is to consider the implications of the observed flattening in the hotspot radio spectrum discussed in Section 4.2.1 and illustrated in Figure 5. We consider two possible mechanisms for producing a flattening in the electron energy distribution at $\gamma \sim 650$. The first mechanism we consider is the dissipation of jet bulk kinetic energy. Dissipation of the jet kinetic energy depletes low-energy particles and produces a turnover in the electron spectrum at a characteristic energy that depends on a number of parameters, including the jet Lorentz factor. The second mechanism we consider is a transition between two distinct acceleration mechanisms.

We note that the inferred value of γ_{min} is only weakly dependent on the assumed Doppler factor δ because Doppler beaming affects the calculation of the magnetic field strength ($B \propto \delta^{-(2+\alpha)/(1+\alpha)}$) as well as the rest frame emission frequency corresponding to γ_{min} ($\nu' \propto \delta^{-1}\nu$). The value of γ_{min} is therefore ∼proportional to $\delta^{1/3}$ (see Table 2).

8.1. Dissipation of Jet Energy

As an illustrative calculation, we consider the dissipation of jet energy in a cold, unmagnetized proton/electron jet. The analysis is effectively done in two steps. First, we use the conservation of energy and particles to calculate the mean Lorentz factor in the hot spot as a function of the jet Lorentz factor. We then relate the mean electron Lorentz factor to the peak Lorentz factor by assuming a particular form for the electron energy distribution. We do not specify the process by which the electrons and protons equilibrate. However, recent particle-in-cell simulations demonstrate that protons and electrons equilibrate in unmagnetized collisionless shocks (Spitkovsky 2008).

The aim of this calculation is to estimate the jet Lorentz factor required to produce a turnover in the electron energy distribution at $\gamma_{min} \sim 650$ if the jet bulk kinetic energy is carried by protons and efficiently transferred to electrons in the hot spot. This analysis can easily be extended to include different jet compositions, different proton to electron energy density ratios and the effects of the magnetic field.

8.1.1. Model Assumptions and Definitions

The relevant quantities are defined as follows: γ is the Lorentz factor of an individual particle measured in the plasma rest frame, γ_p is the electron Lorentz factor at the peak of the electron energy distribution, Γ is the bulk Lorentz factor of

the plasma, $\beta = \sqrt{1 - \Gamma^{-2}}$ is the corresponding plasma speed in units of the speed of light c, θ is the angle between the plasma velocity and the line of sight, $\delta = [\Gamma(1 - \beta \cos \theta)]^{-1}$ is the Doppler factor, $N(\gamma)$ is the number density of electrons per unit Lorentz factor, $\langle \gamma \rangle = \int \gamma N(\gamma)d\gamma / \int N(\gamma)d\gamma$ is the mean Lorentz factor, $n = \int N(\gamma)d\gamma$ is the number density, $\epsilon = (\langle \gamma \rangle - 1) nmc^2$ is the internal energy density, $\rho = nm$ is the rest mass density in the plasma rest frame, p is the pressure, and w is the relativistic enthalpy density. The relativistic enthalpy density is

$$w = \epsilon + p + \rho c^2. \tag{17}$$

We assume the plasma is comprised of electrons (subscript e) and protons (subscript p). Quantities with the subscript 1 refer to the jet plasma, while quantities with a subscript 2 refer to the hotspot plasma.

We assume that the relativistic enthalpy density in the jet is dominated by the rest mass energy density of the proton component, so that $w_1 \approx \rho_{1,p}c^2$. This assumption is valid provided $\langle \gamma \rangle_{1,e} \ll m_p/m_e$.

We assume that the electron population is ultra-relativistic ($\epsilon_e = 3p_e$), and that the proton population in the hotspot plasma is, at best, only mildly relativistic, and can be approximated as a thermal gas ($p_{2,p} = \frac{2}{3}\epsilon_{2,p}$). We further assume that the protons and electrons equilibrate so that $\epsilon_{2,p} = \epsilon_{2,e}$. Hence, the hotspot pressure and enthalpy are $p_2 = \epsilon_{2,e}$ and $w_2 = \rho_2 c^2 + 3\epsilon_{2,e}$.

8.1.2. Conservation Equations

The equations for the conservation of energy and particles are, respectively,

$$A_1 \Gamma_1^2 \beta_1 w_1 = A_2 \Gamma_2^2 \beta_2 w_2 \tag{18}$$

$$A_1 \Gamma_1 \beta_1 n_1 = A_2 \Gamma_2 \beta_2 n_2, \tag{19}$$

where A is the jet cross-sectional area. Dividing Equation (18) by Equation (19), we can write

$$\Gamma_1 \frac{w_1}{\rho_1 c^2} = \Gamma_2 \frac{w_2}{\rho_2 c^2}. \tag{20}$$

8.1.3. The Peak Lorentz Factor

Combining Equation (20) with our model assumptions described above, we find

$$\Gamma_1 \approx \Gamma_2 \left(1 + \frac{3\epsilon_{2,e}}{\rho_2 c^2} \right) \tag{21}$$

$$\approx \Gamma_2 \left(1 + 3 \frac{m_e}{m_p} \langle \gamma \rangle \right), \tag{22}$$

where we have made the substitution $\rho_2 \approx n_p m_p$ and $\epsilon_{2,e} = \langle \gamma \rangle n_e m_e c^2$.

Let us introduce the parameter $\chi \equiv \langle \gamma \rangle / \gamma_p$ which is the ratio of the mean electron Lorentz factor in the hot spot ($\langle \gamma \rangle$) to the electron Lorentz factor at the peak of the electron energy distribution (γ_p). Then

$$\gamma_p = \frac{1}{3} \frac{m_p}{m_e} \left(\frac{\Gamma_1}{\Gamma_2} - 1 \right) \chi^{-1}. \tag{23}$$

In order to estimate the parameter χ, we assume that the electron distribution below γ_p can be approximated by the
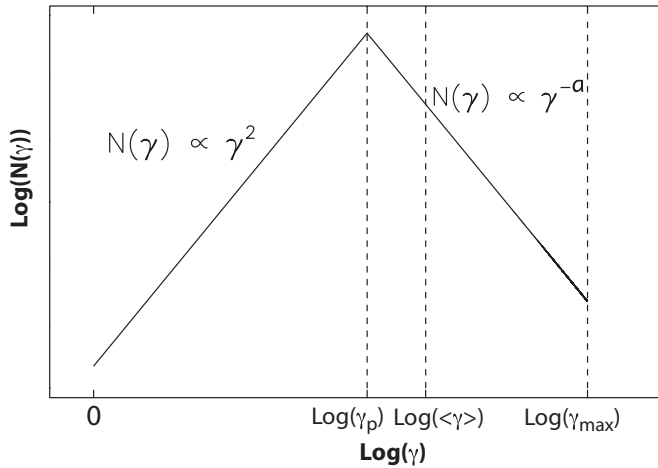
Figure 9. Plot of the assumed form of the electron energy distribution used to relate the mean of the distribution $\langle\gamma\rangle$ to the mode γ_p (see Equations (24) and (25)). In Section 4.2, when modeling the hotspot spectrum, we approximated the electron energy distribution with a broken power law between $\gamma_{\min}$ and $\gamma_{\max}$, and number density set to zero outside this range. Here we assume that initially the (injected) electron spectrum is a single (unbroken) power law between γ_p and $\gamma_{\max}$, with $N(\gamma) \propto \gamma^2$ below γ_p. The instantaneous cutoff at $\gamma_{\min}$ used for spectral modeling is an approximation to the turnover in the electron energy distribution. We identify $\gamma_{\min}$ with the peak of the electron energy distribution, which here we define as γ_p.

low-energy tail of a relativistic Maxwellian, and above γ_p the electron distribution (before cooling via synchrotron emission) is a power law, extending from the peak to a maximum Lorentz factor $\gamma_{\max}$ (see Figure 9):

$$N(\gamma) = \begin{cases} K_e \gamma_p^{-(a+2)} \gamma^2 & 1 < \gamma < \gamma_p \\ K_e \gamma^{-a} & \gamma_p < \gamma < \gamma_{\max} \\ 0 & \gamma > \gamma_{\max}. \end{cases} \quad (24)$$

Using this particular form for the energy distribution, the value of χ is a function of the three parameters a, γ_p and $\gamma_{\max}$. If $a = 2$, the ratio of mean Lorentz factor to the peak Lorentz factor reduces to the following simple algebraic form:

$$\chi \approx \frac{3}{16} + \frac{3}{4}\ln\left(\frac{\gamma_{\max}}{\gamma_p}\right) \quad (25)$$

provided $\gamma_p \gg 1$. From our analysis of the spectrum of the northern hot spot of PKS 1421−490 in Section 4.2.4, we have $\gamma_p \approx 650$, $\gamma_{\max} \approx 1.2 \times 10^5$, and $a = 2.06$, so that $\chi \approx 4$. Therefore, in order to produce a turnover in the electron energy distribution at $\gamma_{\min} \sim 650$, the jet must have a bulk Lorentz factor $\Gamma_1 \gtrsim 5$. This value of the jet Lorentz factor is consistent with jet Lorentz factors inferred from modeling the radio to X-ray spectra of quasar jets on kpc scales (Tavecchio et al. 2000; Schwartz et al. 2006; Kataoka & Stawarz 2005). If $\Gamma_2 > 1$, or the jet contains some fraction of positron/electron pairs, or the electrons do not reach equilibrium with the protons, or we consider the effect of the magnetic field, then the energy requirements increase, and the estimate of Γ_1 will be greater.

It was noted in Section 1 that while only a small number of hot spots have provided direct estimates of $\gamma_{\min}$, they are all distributed around a value of $\gamma_{\min} \approx 600$ to within a factor of 2 (excluding the value $\gamma_{\min} \sim 10^4$ indirectly estimated by Blundell et al. (2006)). The value of the parameter χ is weakly dependent on the electron spectrum, and in general should be within the range $\chi \sim 2$–6. Therefore, dissipation of

bulk kinetic energy associated with relativistic proton/electron jets with bulk Lorentz factors of order $\Gamma_1 \gtrsim 5$ can provide a natural explanation for the inferred turnovers in electron spectra at $\gamma_{\min} \sim 300 - 1000$.

Our analysis indicates that the value of $\gamma_{\min} \sim 10^4$ inferred by Blundell et al. (2006) for the hot spot of the radio galaxy 6C0905+3955 would require a jet Lorentz factor $\Gamma_{\text{jet}} \gtrsim 16\chi + 1$. If $\chi \gtrsim 2$ (note that $\alpha \sim 0.7$ for this hot spot, and the synchrotron spectrum extends from radio through to soft X-ray frequencies (Erlund et al. 2008)), then the required jet Lorentz factor is $\Gamma_{\text{jet}} \gtrsim 35$.

8.1.4. Electron/Positron Jet

Let us now consider the case of a pure electron/positron jet. In this case, assuming an ultrarelativistic equation of state in the jet and hot spot, the ratio of Equations (18) and (19) implies

$$\Gamma_1 \gtrsim \frac{\langle\gamma\rangle_{2,e}}{\langle\gamma\rangle_{1,e}}. \quad (26)$$

Uchiyama et al. (2005) estimate a mean Lorentz factor of $\langle\gamma\rangle_{1,e} \approx 50$ in the jet of PKS 0637–752. If a similar mean Lorentz factor applies to the jet of PKS 1421−490 then the required jet bulk Lorentz factor is $\Gamma_1 \gtrsim 50$.

8.2. Pre-acceleration: Cyclotron Resonant Absorption?

We now consider an alternative explanation for the flattening of the electron energy distribution. The observed change in slope may be the result of a transition between two different acceleration mechanisms: a pre-acceleration process producing a relatively flat electron spectrum at low energy, and diffusive shock acceleration acting at higher energy producing an electron distribution $N(\gamma) \propto \gamma^{-a}$ with $a \sim 2$. We have not modeled the spectrum in terms of such a scenario, but this model cannot yet be ruled out.

One interesting candidate for the pre-acceleration mechanism is that described by Hoshino et al. (1992) and Amato & Arons (2006). They have shown that in a relativistic, magnetized, collisionless shock with an electron–positron–proton plasma there can be efficient transfer of energy from protons to leptons via the resonant emission and absorption of electromagnetic waves at high harmonics of the proton cyclotron frequency. This process produces a particle distribution described by a relativistic Maxwell distribution at low energies ($\gamma < \Gamma_{\text{jet}}$) and a relatively flat ($a < 2$) power-law component extending from $\sim \Gamma_{\text{jet}}$ to $\sim \Gamma_{\text{jet}}(m_p/m_e)$. The electron energy index of the power-law component is sensitive to the plasma composition. The theoretical maximum Lorentz factor attained via this acceleration mechanism ($\sim \Gamma_{\text{jet}}(m_p/m_e)$) is set by resonance with the fundamental proton cyclotron frequency. However, the upper cutoff energy determined from the results of particle-in-cell simulations is somewhat lower than the theoretical maximum (Amato & Arons 2006). Therefore, the observed flattening in the hotspot radio spectrum may be associated with a transition between the cyclotron resonant absorption mechanism and diffusive shock acceleration. Stawarz et al. (2007) have suggested this interpretation for the hotspot spectra in Cygnus A.

9. CONCLUSIONS

LBA imaging of the $z = 0.663$ broadline radio galaxy PKS 1421−490 has revealed a compact (400 pc diameter), high

surface brightness hot spot at a projected distance of ∼40 kpc from the AGN. The isotropic X-ray luminosity of the hot spot, $L_{2-10\,keV} = 3 \times 10^{44}$ ergs s^{-1}, is comparable to the isotropic X-ray luminosity of the entire X-ray jet of PKS 0637−752, and the peak radio surface brightness is hundreds of times greater than that of the brightest hot spot in Cygnus A. We successfully modeled the radio to X-ray spectral energy distribution using a standard one-zone synchrotron self-Compton model with a near equipartition magnetic field strength of 3 mG. There is a strong brightness asymmetry between the approaching and receding hotspots, and the hot spot spectrum remains flat ($\alpha \approx 0.5$) well beyond the predicted cooling break for a 3 mG magnetic field, indicating that the hotspot emission may be Doppler beamed. We suggest that a high plasma velocity beyond the terminal jet shock could be the result of a dynamically important magnetic field in the jet, resulting in Doppler boosted hotspot emission. However, some aspects of the hotspot morphology may argue against an interpretation involving significant Doppler beaming. LBA observations at 1.4 GHz will be required to further investigate the hotspot morphology.

There is a change in the slope of the hotspot radio spectrum at GHz frequencies. We successfully modeled this feature by incorporating a cutoff in the electron energy distribution at $\gamma_{min} \sim 650$ (assuming a Doppler factor of unity). If the hotspot emission is Doppler beamed and the Doppler factor δ, the low-energy cutoff is $\gamma_{min} \approx 650 \; \delta^{1/3}$. We have made use of the equations for the conservation of energy and particles in an unmagnetized proton/electron jet to obtain a general expression that relates the peak in the hotspot electron energy distribution to the jet bulk Lorentz factor. We have shown that a sharp decrease in electron number density below a Lorentz factor of about 650 would arise from the dissipation of bulk kinetic energy in an electron/proton jet with a bulk Lorentz factor $\Gamma_{jet} \gtrsim 5$. This value of the jet Lorentz factor is consistent with jet Lorentz factors inferred from modeling the radio to X-ray spectra of quasar jets on kpc scales (Tavecchio et al. 2000; Schwartz et al. 2006; Kataoka & Stawarz 2005). These results are of particular interest given that similar values of γ_{min} have been estimated for several other hotspots. Our analysis indicates that the value of $\gamma_{min} \sim 10^4$ inferred by Blundell et al. (2006) for the hot spot of the radio galaxy 6C0905+3955 would require a jet Lorentz factor $\Gamma_{jet} \gtrsim 35$.

An alternative explanation for the low-frequency flattening in the radio spectrum of the northern hot spot of PKS 1421−490 may be that it is associated with the transition between a pre-acceleration mechanism, such as the cyclotron resonant process described by Hoshino et al. (1992) and Amato & Arons (2006), and diffusive shock acceleration.

Future LBA observations at 1.4 GHz will help us to constrain the low-energy end of the electron energy distribution, and infrared observations are required to constrain the high-frequency end of the synchrotron spectrum. More sophisticated models of the electron energy distribution will be required in future studies, to test the hypothesis that the flattening in the radio spectrum is associated with a transition between two distinct acceleration mechanisms.

APPENDIX

EQUATIONS FOR SYNCHROTRON AND SSC MODEL FLUX DENSITY

A.1. Angle-Averaged Synchrotron Flux Density for an Arbitrary Electron Energy Distribution

The standard expressions for the synchrotron spectrum produced by an arbitrary electron energy distribution contain a dependence on the angle between the line of sight and the magnetic field (see e.g., Worrall & Birkinshaw 2006). If the magnetic field direction changes significantly throughout the volume in which the observed flux is produced, it is appropriate to use the angle-averaged emission spectrum to model the source. In this appendix, we present a formal way of calculating the angle-averaged synchrotron spectrum for an arbitrary electron energy distribution. We then give the expression used in calculating the flux density from the volume-averaged shock distribution described in the text.

Let $N(\gamma)$ be the number density per unit Lorentz factor of relativistic electrons defined as nonzero between some minimum and maximum Lorentz factors γ_{min} and γ_{max} in a magnetic field of flux density B. Further, define the nonrelativistic gyrofrequency as Ω_0, and the classical electron radius as r_e. Written in SI units, $\Omega_0 = \frac{q_e B}{m_e}$, and in cgs units, $\Omega_0 = q_e B / m_e c$, where q_e and m_e are the electron charge and mass, respectively. Let $y = (4\pi/3)\Omega_0^{-1}\gamma^{-2}$. The angle-averaged synchrotron emissivity (valid in both SI and cgs units) is

$$\langle j_\nu \rangle = \frac{1}{4\pi} \int_{4\pi} j_\nu d\Omega \tag{A1}$$

$$= \left(\frac{m_e r_e c}{4\pi^{1/2}}\right) \nu^{1/2} \Omega_0^{1/2} \int_{y_1}^{y_2} y^{-3/2} N(\gamma(y))\bar{F}(y)dy, \tag{A2}$$

where

$$\bar{F}(y) = \int_0^{\pi/2} F\left(\frac{y}{\sin\psi}\right) \sin^2\psi \, d\psi \tag{A3}$$

$$= y \int_y^\infty \left(1 - \frac{y^2}{t^2}\right)^{1/2} K_{5/3}(t)dt \tag{A4}$$

and the synchrotron function $F(x) = x \int_x^\infty K_{5/3}(z)dz$, where $K_{5/3}(z)$ is the modified Bessel function of order 5/3. The integration limits on y are given by

$$y_1 = \frac{4\pi}{3}\frac{\nu}{\Omega_0}\gamma_{max}^{-2} = \nu/\nu_2 \tag{A5}$$

$$y_2 = \frac{4\pi}{3}\frac{\nu}{\Omega_0}\gamma_{min}^{-2} = \nu/\nu_1, \tag{A6}$$

where ν_1 and ν_2 are characteristic frequencies corresponding to $\gamma_{\min}$ and $\gamma_{\max}$, namely, $\frac{3}{4\pi}\Omega_0\gamma_{\min,\max}^2$.

Using the volume-averaged shock distribution function $\bar{N}(\gamma(y))$ defined by Equations (3) and (4), the angle-averaged emission spectrum is

$$\langle F_\nu \rangle = \frac{\delta^{(a+3)/2}(1+z)^{(3-a)/2}V}{D_L^2}A(a)\nu^{-a/2}\nu_b^{1/2}A_{\mathrm{syn}}$$
$$\times \int_{\nu/\nu_2}^{\nu/\nu_1} y^{\frac{a-2}{2}}\bar{F}(y)\,g\left(y,\frac{\nu}{\nu_b}\right)dy, \qquad (A7)$$

where

$$g\left(y,\frac{\nu}{\nu_b}\right) = \begin{cases} 1-\left[1-\left(\frac{\nu}{y\nu_b}\right)^{1/2}\right]^{a-1} & y > \frac{\nu}{\nu_b} \\ 1 & y < \frac{\nu}{\nu_b} \end{cases} \qquad (A8)$$

$$\nu_{1,b,2} = \frac{\delta}{(1+z)}\frac{3}{4\pi}\Omega_0\gamma_{\min,b,\max}^2 \qquad (A9)$$

$$A_{\mathrm{syn}} = K_e\Omega_0^{\frac{a+1}{2}} \qquad (A10)$$

$$A(a) = \frac{r_e m_e c\, 3^{a/2}}{(a-1)\,2^{a+2}\,\pi^{\frac{a+1}{2}}}. \qquad (A11)$$

The shape of the model synchrotron spectrum is determined by the parameters ν_1, ν_b, ν_2, and a. The amplitude is governed by the parameter A_{syn}. In Equation (A7), we have assumed the emission is produced by plasma flowing at a relativistic speed βc at an angle θ to the line of sight with the corresponding Lorentz factor $\Gamma = \left(1-\beta^2\right)^{-1/2}$ and Doppler factor $\delta = [\Gamma(1-\beta\cos\theta)]^{-1}$ through a stationary volume or pattern, so that $F_\nu \propto \delta^{(a+3)/2}$ as appropriate for extragalactic jets (Lind & Blandford 1985). If the volume in which the flux is produced is moving relativistically, an extra factor of δ enters, so that the leading factor of $\delta^{(a+3)/2}$ in Equation (A7) becomes $\delta^{(a+5)/2}$.

To calculate the model synchrotron spectrum, we first specify a source volume V, Doppler factor δ, redshift z, and corresponding luminosity distance D_L. We then specify lab frame values for the critical frequencies ν_1, ν_b, and ν_2 and the observation frequency ν. Finally, we specify the synchrotron amplitude A_{syn} and calculate the spectrum numerically using Equation (A7).

A.2. Synchrotron Self-Compton Flux Density

Let ϵ_s be the inverse Compton scattered photon energy, ϵ_i the soft-photon energy, $n(\epsilon_i)$ the number density of soft photons per unit energy, $N(\gamma)$ the number density of relativistic electrons per unit Lorentz factor and σ_T the Thompson cross section. The inverse Compton emissivity (in the Thompson limit) from an isotropic distribution of relativistic electrons in an isotropic soft photon field is given by

$$j_{\epsilon_s} = \frac{3c\sigma_T}{16\pi}\epsilon_s\int_0^\infty \frac{n(\epsilon_i)}{\epsilon_i}\left[\int_{\gamma_{\min}}^{\gamma_{\max}}\frac{N_e(\gamma)}{\gamma^2}F_C(q)d\gamma\right]d\epsilon_i, \qquad (A12)$$

where

$$q = \frac{\epsilon_s}{4\epsilon_i\gamma^2} \qquad (A13)$$

and

$$F_C(q) = 2q\ln(q) + q + 1 - 2q^2 \qquad (A14)$$

(e.g., Blumenthal & Gould 1970). This expression is valid for any particle distribution and any photon distribution, provided they are both isotropic. Changing the integration variable from γ to q, we obtain

$$j_{\epsilon_s} = \frac{3c\sigma_T}{2^6\pi}\epsilon_s^{3/2}\int_0^\infty \frac{n(\epsilon_i)}{\epsilon_i^{3/2}}\left[\int_{q2}^{q1}\frac{N(\gamma)}{\gamma^2}q^{-3/2}F_C(q)dq\right]d\epsilon_i, \qquad (A15)$$

where

$$q_{1,2} = \frac{\epsilon_s}{4\epsilon_i\gamma_{\min,\max}^2}. \qquad (A16)$$

Using the broken power-law distribution described by Equations (3) and (4) and expressing it in terms of the variable q, we find

$$F_\nu^{\mathrm{ssc}} = \left(\frac{9\cdot 2^{(a-3)}R\,\sigma_T}{a-1}\right)\nu^{-a/2}A_{\mathrm{ssc}}\int_{\nu_1}^{\nu_2}\nu_i^{(a-2)/2}F_{\nu_i}^{\mathrm{syn}}$$
$$\times\left[\int_{q2}^{q_1}q^{a/2}F_C(q)g\left(\frac{q_b}{q}\right)dq\right]d\nu_i, \qquad (A17)$$

where

$$A_{\mathrm{ssc}} = K_e\gamma_b$$
$$q_b = \frac{\epsilon_s}{4\epsilon_i\gamma_b^2} \qquad (A18)$$

$$g\left(\frac{q_b}{q}\right) = \begin{cases} 1-\left(1-\left(\frac{q_b}{q}\right)^{1/2}\right)^{a-1} & q > q_b \\ 1 & q < q_b \end{cases} \qquad (A19)$$

and $F_{\nu_i}^{\mathrm{syn}}$ is calculated using Equation (A7). In Equation (A17), we have assumed

$$\int n(\epsilon_i')dV' = \frac{3\pi}{h^2\nu_i'c}Rj_{\nu_i'}^{'\mathrm{syn}}V' \qquad (A20)$$

$$= \frac{3\pi R}{h^2\nu_ic}\frac{F_{\nu_i}^{\mathrm{syn}}D_L^2}{\delta(1+z)} \qquad (A21)$$

as appropriate for a spherical region of homogenous plasma. In the above expression, ϵ_i' and ν_i' are the incident photon energy and frequency in the rest frame of the plasma, and $j_{\nu_i}^{\mathrm{syn}}$ is the synchrotron emissivity at frequency ν_i' in the rest frame of the plasma.

We calculate the synchrotron self-Compton spectrum by specifying the value of A_{ssc} along with the best-fit values for A_{syn}, ν_1, ν_b, and ν_2 determined from fitting the synchrotron spectrum. The spectrum is calculated using Equations (A17). Together, the five parameters ν_1, ν_b, ν_2, A_{syn}, and A_{ssc} allow the parameters K_e, B, $\gamma_{\min}$, γ_b, and $\gamma_{\max}$ to be determined.

REFERENCES

Aloy, M. A., Ibáñez, J. M., Martí, J. M., Gómez, J.-L., & Müller, E. 1999, ApJ, 523, L125
Amato, E., & Arons, J. 2006, ApJ, 653, 325
Bałucińska-Church, M., Ostrowski, M., Stawarz, Ł., & Church, M. J. 2005, MNRAS, 357, L6
Belsole, E., Worrall, D. M., & Hardcastle, M. J. 2006, MNRAS, 366, 339
Blumenthal, G. R., & Gould, R. J. 1970, Rev. Mod. Phys., 42, 237
Blundell, K. M., Fabian, A. C., Crawford, C. S., Erlund, M. C., & Celotti, A. 2006, ApJ, 644, L13

Bridle, A. H., Hough, D. H., Lonsdale, C. J., Burns, J. O., & Laing, R. A. 1994, AJ, 108, 766

Brunetti, G., Mack, K.-H., Prieto, M. A., & Varano, S. 2003, MNRAS, 345, L40

Campbell-Wilson, D., & Hunstead, R. W. 1994, Proc. Astron. Soc. Aust., 11, 33

Carilli, C. L., Dreher, J. W., Perley, R. A., Leahy, P., & Muxlow, T. 1988, BAAS, 20, 734

Carilli, C. L., Kurk, J. D., van der Werf, P. P., Perley, R. A., & Miley, G. K. 1999, AJ, 118, 2581

Carilli, C. L., Perley, R. A., Dreher, J. W., & Leahy, J. P. 1991, ApJ, 383, 554

Cheung, C. C., Wardle, J. F. C., & Chen, T. 2005, ApJ, 628, 104

Dennett-Thorpe, J., Bridle, A. H., Scheuer, P. A. G., Laing, R. A., & Leahy, J. P. 1997, MNRAS, 289, 753

de Young, D. S. 2002, The Physics of Extragalactic Radio Sources (Chicago, IL: Univ. Chicago Press)

Double, G. P., Baring, M. G., Jones, F. C., & Ellison, D. C. 2004, ApJ, 600, 485

Ekers, J. A. 1969, Aust. J. Phys. Astrophys. Suppl., 7, 3

Erlund, M. C., Fabian, A. C., & Blundell, K. M. 2008, MNRAS, 386, 1774

Francis, P. J., Hewett, P. C., Foltz, C. B., Chaffee, F. H., Weymann, R. J., & Morris, S. L. 1991, ApJ, 373, 465

Gambill, J. K., Sambruna, R. M., Chartas, G., Cheung, C. C., Maraschi, L., Tavecchio, F., Urry, C. M., & Pesce, J. E. 2003, A&A, 401, 505

Gelbord, J. M., et al. 2005, ApJ , L75 (G05)

Georganopoulos, M., & Kazanas, D. 2003, ApJ, 589, L5

Gopal-Krishna , Biermann, P. L., & Wiita, P. J. 2004, ApJ, 603, L9

Hardcastle, M. J. 2001, A&A, 373, 881

Hardcastle, M. J. 2003, New Astron. Rev., 47, 649

Hardcastle, M. J., Alexander, P., Pooley, G. G., & Riley, J. M. 1998, MNRAS, 296, 445

Hardcastle, M. J., Birkinshaw, M., & Worrall, D. M. 2001, MNRAS, 323, L17

Hardcastle, M. J., Birkinshaw, M., Cameron, R. A., Harris, D. E., Looney, L. W., & Worrall, D. M. 2002, ApJ, 581, 948

Hardcastle, M. J., Harris, D. E., Worrall, D. M., & Birkinshaw, M. 2004, ApJ, 612, 729

Harris, D. E., et al. 2000, ApJ, 530, L81

Heavens, A. F., & Meisenheimer, K. 1987, MNRAS, 225, 335

Hoshino, M., Arons, J., Gallant, Y. A., & Langdon, A. B. 1992, ApJ, 390, 454

Ishwara-Chandra, C. H., & Saikia, D. J. 2000, MNRAS, 317, 658

Jeyakumar, S., & Saikia, D. J. 2000, MNRAS, 311, 397

Jones, T. W., & Odell, S. L. 1977, A&A, 61, 291

Kataoka, J., & Stawarz, Ł. 2005, ApJ, 622, 797

Komissarov, S. S., & Falle, S. A. E. G. 1996, Energy Transp. Radio Galaxies Quasars, 100, 327

Large, M. I., Mills, B. Y., Little, A. G., Crawford, D. F., & Sutton, J. M. 1981, MNRAS, 194, 693

Lazio, T. J. W., Cohen, A. S., Kassim, N. E., Perley, R. A., Erickson, W. C., Carilli, C. L., & Crane, P. C. 2006, ApJ, 642, L33

Leahy, J. P., Muxlow, T. W. B., & Stephens, P. W. 1989, MNRAS, 239, 401

Lind, K. R., & Blandford, R. D. 1985, ApJ, 295, 358

Linfield, R. P., et al. 1989, ApJ, 336, 1105

Lovell, J. E. J. 1997, PhD thesis, Univ. Tasmania

Marscher, A. P. 1988, ApJ, 334, 552

Marshall, H. L., et al. 2005, ApJS, 156, 13

Meisenheimer, K. 2003, New Astron. Rev., 47, 495

Meisenheimer, K., Yates, M. G., & Roeser, H.-J. 1997, A&A, 325, 57

Norman, M. L. 1996, Energy Transp. Radio Galaxies Quasars, 100, 319

Preston, R. A., et al. 1989, AJ, 98, 1

Prieto, M. A., Brunetti, G., & Mack, K.-H. 2002, Science, 298, 193

Rayner, D. P., Norris, R. P., & Sault, R. J. 2000, MNRAS, 319, 484

Roeser, H.-J., & Meisenheimer, K. 1987, ApJ, 314, 70

Schwartz, D. A., et al. 2006, ApJ, 640, 592

Shepherd, M. C. 1997, Astron. Data Anal. Soft. Syst. VI, 125, 77

Spitkovsky, A. 2008, ApJ, 673, L39

Stawarz, Ł., Cheung, C. C., Harris, D. E., & Ostrowski, M. 2007, ApJ, 662, 213

Tavecchio, F., Maraschi, L., Sambruna, R. M., & Urry, C. M. 2000, ApJ, 544, L23

Tavecchio, F., Cerutti, R., Maraschi, L., Sambruna, R. M., Gambill, J. K., Cheung, C. C., & Urry, C. M. 2005, ApJ, 630, 721

Tsang, O., & Kirk, J. G. 2007, A&A, 463, 145

Tregillis, I. L., Jones, T. W., & Ryu, D. 2001, ApJ, 557, 475

Uchiyama, Y., Urry, C. M., Van Duyne, J., Cheung, C. C., Sambruna, R. M., Takahashi, T., Tavecchio, F., & Maraschi, L. 2005, ApJ, 631, L113

Urry, C. M., & Padovani, P. 1995, PASP, 107, 803

Wardle, J. F. C. 1977, Nature, 269, 563

Wardle, J. F. C., Homan, D. C., Ojha, R., & Roberts, D. H. 1998, Nature, 395, 457

Wills, B. J. 1975, Aust. J. Phys. Astrophys. Suppl., 38, 1

Worrall, D. M., & Birkinshaw, M. 2006, Lect. Notes Phys., 693, 39